J. Fluid Mech. (2024), *vol*. 987, A20, doi:10.1017/jfm.2024.372

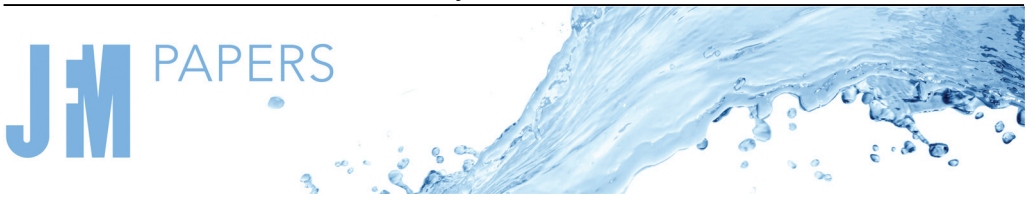

Three-dimensional flow around and through a porous screen

Olivier C. Marchand[1],†, **Sophie Ramananarivo**[1], **Camille Duprat**[1] and **Christophe Josserand**[1]

[1]Laboratoire d'Hydrodynamique (LadHyX), UMR7646, CNRS, École polytechnique, Institut Polytechnique de Paris, 91120 Palaiseau, France

(Received 1 March 2023; revised 22 January 2024; accepted 3 April 2024)

We investigate the three-dimensional (3-D) flow around and through a porous screen for various porosities at high Reynolds number $Re = O(10^4)$. Historically, the study of this problem has been focused on two-dimensional cases and for screens spanning completely or partially a channel. Since many recent problems have involved a porous object in a 3-D free flow, we present a 3-D model initially based on Koo & James (*J. Fluid Mech.*, vol. 60, 1973, pp. 513–538) and Steiros & Hultmark (*J. Fluid Mech.*, vol. 853, 2018 pp. 1–11) for screens of arbitrary shapes. In addition, we include an empirical viscous correction factor accounting for viscous effects in the vicinity of the screen. We characterize experimentally the aerodynamic drag coefficient for a porous square screen composed of fibres, immersed in a laminar air flow with various solidities and different angles of attack. We test various fibre diameters to explore the effect of the space between the pores on the drag force. Using PIV and hot wire probe measurements, we visualize the flow around and through the screen, and in particular measure the proportion of fluid that is deviated around the screen. The predictions from the model for drag coefficient, flow velocities and streamlines are in good agreement with our experimental results. In particular, we show that local viscous effects are important: at the same solidity and with the same air flow, the drag coefficient and the flow deviations strongly depend on the Reynolds number based on the fibre diameter. The model, taking into account 3-D effects and the shape of the porous screen, and including an empirical viscous correction factor that is valid for fibrous screens may have many applications including the prediction of water collection efficiency for fog harvesters.

Key words: flow-structure interactions, drag reduction, porous media

† Email address for correspondence: olivier.marchand@ladhyx.polytechnique.fr

1. Introduction

The flow around porous structures has been largely investigated throughout the recent decades and has many engineering applications. It can be applied to parachute problems for the determination of drag and stability (Sarpkaya & Lindsey 1990; Johari & Desabrais 2005), to vertical axis wind turbines (Ayati *et al.* 2019) as well as to blockage correction in wind tunnels (Steiros, Bempedelis & Cicolin 2022). Laws & Livesey (1978) highlighted the possibility of using screens in flow to control the velocity distribution and change the flow direction. The understanding and improvement of the water collection of fog harvesters in arid regions require a quantitative description of the flow in the vicinity of the net (Regalado & Ritter 2016; Moncuquet *et al.* 2022). Furthermore, such a quantitative description may provide a first step in the physical understanding of respiratory flows in the presence of a face mask, as used to reduce the propagation of an airborne virus such as SARS-CoV-2 (Mittal, Ni & Seo 2020; Bourrianne *et al.* 2021). In these cases, the flow can either pass through the porous net or mask, or is deviated around or through the leaks. More generally, there may be an interest in reducing the constraints exerted on high panels or masts exposed to a flow for safety reasons, leading to an increased interest in large porous structures as mentioned by Giannoulis *et al.* (2012). In some buildings, a permeable layer is added at a certain distance from the façade for energy efficiency reasons or to block a part of the sun rays. Also, windbreak panels are usually used in industry and power plants to control wind and dust pollution. In these cases an estimation of the cladding wind load is useful information for architects and engineers (Pomaranzi *et al.* 2020). Furthermore, the modelling of the interaction of flow with arrays of fibres and the prediction of the corresponding drag can be helpful to understand the mechanism of filter feeding for numerous marine organisms for which arrays of bristles move in water to capture food particles (see Cheer & Koehl 1987; Hood, Jammalamadaka & Hosoi 2019).

The main physical characteristics of the screen involved in flow resistance is the porosity and the permeability. For very thin porous screens, the porosity can be represented by the solidity, which is the ratio between the solid surface area and the total surface area of the screen. The permeability is defined as the parameter relating the pressure gradient within a porous media to the local velocity of the flow, depending on the geometry of the pores. The porosity effects on pressure drop across porous screens and on drag force has largely been investigated, both theoretically and experimentally, whereas the permeability effect is much less understood, especially for very thin porous structures. However, some recent work at low Reynolds numbers has been conducted highlighting its influence: in particular, Ledda *et al.* (2018) has shown that the permeability has a strong effect on the wake characteristics, and Pezzulla *et al.* (2020) has demonstrated that the drag coefficient of the screen depends on the permeability. On the other hand, Steiros & Hultmark (2018) have developed a model to predict the drag coefficient for two-dimensional (2-D) perforated plates as a function of the solidity only. Although they obtained a good agreement with experimental data, this approach does not take explicitly into account the Reynolds number based on the scale of the pores, while it is known that the behaviour of the flow in the vicinity of the screen depends on the specific geometry of the pores as well as the material and thickness of the screen (see § 4.1).

Several approaches have been adopted to model the flow. For instance, Carvajal *et al.* (2020) used three-dimensional (3-D) numerical simulations to access the aerodynamic characteristics during fog collection and model the net as a porous medium using Darcy's law, whereas de Dios Rivera (2011) used the superposition principle applied to a flow passing around a solid plate and a flow forced to pass through the net to find an approximation of the velocity at the screen. The difficulty of the problem lies in the

multiscale physical phenomena, from the characteristic scale of the flow around the screen that is of order 0.1 to 1 m to that of the flow through the screen (i.e. the pore size) that is of order $O(10^{-3})$ to $O(10^{-6})$ m; the scale of the Reynolds number thus varies from low Reynolds numbers at the pore scale (of order $O(10^{-1})$) to large ones at the net scale (of order $O(10^{6})$). Therefore, the physical mechanisms of the whole system cannot be easily captured by a numerical simulation resolving all scales as noticed by Shklyar & Arbel (2008), and the method generally used consists in modelling the porous surface as an imaginary interface where transfers of mass and momentum occur. The macroscopic jump laws for the velocities and pressure at the interface are deduced from a microscopic model at the vicinity of the screen where the fluid is generally governed by the steady Stokes equations. This can be obtained by periodic homogenization theory as done by Zampogna & Gallaire (2020) and has been recently used for permeable shells by Ledda *et al.* (2021). However, these methods introduce some parameters like the permeability of the porous surface that are difficult to measure experimentally, although they could be obtained using pore-scale simulation.

We aim here at predicting the drag coefficient of elevated porous panels of arbitrary shape placed in a laminar flow, and the corresponding flow through the structure, in conditions relevant for many applications (e.g. fog harvesting). We focus on porous screens composed of fibres, but the model can be applied without major changes to other kinds of porous screens. Experimentally, we consider rectangular meshes of woven fibres, with fibre diameters between 6.0 µm and 1.9 mm and with typical pore sizes of the order of 10 µm to 1.0 cm, placed in a uniform laminar flow of velocity varying from 0.5 to 13 m s^{-1} with three orientation angles. For a given fibre diameter, we vary the porosity of the screen by changing the fibres arrangements and pore sizes; conversely, we study screens of the same porosity but different fibre diameters, in order to study the effect of the screen porosity and the flow around or through the screen, as well as the effect of the microstructure, i.e. of the local pore Reynolds number associated to the flow through the individual pores. We measure the drag coefficient and perform velocimetry measurements of the flow around the screen with particle image velocimetry (PIV) and a hot wire probe.

Our goal is to obtain a model of the flow for porous surfaces based only on the porosity, the large-scale geometry of the screen and the Reynolds number at the scale of the holes (instead of the permeability), which are easy to access. From this model, we wish to obtain values of the drag coefficient as well as the proportion of the flow that is deviated around the screen. We focus on the model first proposed by Taylor (1944) and used by numerous authors (O'Neill 2006), which consists in considering the screen as a distribution of sources. This approach has been adopted by Koo & James (1973) who proposed a 2-D mathematical model for a screen confined in a channel with two parallel boundaries. Recently, Steiros & Hultmark (2018) derived the drag coefficient of a porous plate based partially on Koo & James (1973) and 2-D potential flow. Since their prediction showed a good agreement with their experimental data, here we propose to extend the model of Koo & James (1973) to a 3-D free flow, keeping the same main hypothesis but taking into account the shape of the screen, 3-D effects and the base suction effect considered by Steiros & Hultmark (2018). We then derive the equations to predict the drag coefficient following the method proposed by Steiros & Hultmark (2018), and discuss the limits of this approach. While the pressure jump derived following the method of Taylor (1944) and Steiros & Hultmark (2018) is based on clear physical assumptions, it fails to reproduce the viscous effects observed experimentally, i.e. finite pore Reynolds number. We thus incorporate in the model the empirical law of Brundrett (1993) for the pressure jump. We compare the prediction of the drag coefficient and of the proportion of deviated fluid for

various porosities and Reynolds number based on the fibres' diameter to our experimental results (both with the theoretical and empirical law of the pressure jump).

Furthermore, very few studies report measurements on the drag coefficient for elevated panels with different angles of attack (to the best of our knowledge only Prandtl & Flachsbart 1932; Letchford 2001). We therefore also study the flow for arbitrary angle of attacks and compare our theoretical prediction with experimental data for two angles of attack (65° and 43°). Finally, we discuss the asymptotic behaviour of the model at solidities close to 1.

2. Experiments

We measure experimentally the drag coefficient for a series of porous planar structures consisting of regularly woven nylon yarns in a square mesh and other types of meshes like rod screens (parallel fibres), of size $L = 10\,\text{cm} \times 10\,\text{cm}$. The characteristics of the porous screens as well of their solidity are detailed in Appendix C, and we also present a synthesis in table 1. The solidity s is defined as the ratio between the solid surface area of the screen to its total area S_p. We also characterize the drag coefficient for a classical surgical face mask for which the physical characteristics such as the fibre diameter and the solidity are taken from Monjezi & Jamaati (2021) and Du *et al.* (2021) (screen P9 in table 1). The porous structure is held in a planar configuration by a square frame with a width of 0.5 cm (that is 2.1 % of the surface area of the porous structure), representing a small portion (7.6 %) of the total cross-section of the laminar flow generated by the wind tunnel. Following Letchford (2001), the square frame is fixed on a 21.5 cm high mast to avoid boundary layer effects. The set-up is shown in figure 1.

A force balance (SIXAXES, FX2.6, No 1026, ±5 N, sensitivity of ±0.001 N) is used to measure the force applied to the whole system. The laminar airflow is generated by an open jet wind tunnel with a square test section of width 40 cm. We also perform experiments on inclined porous screens; in that case eight different velocities have been used. For both cases, the velocities vary from 0.5 to 13 m s^{-1}. We can thus define the (global) Reynolds number of the problem as

$$Re = \frac{L_0 v_0}{\nu}, \tag{2.1}$$

where v_0 is the uniform velocity of the flow far upstream of the screen, L_0 its typical size and ν the kinematic viscosity of the fluid (the air for the configurations considered here, so $\nu = 15.6 \times 10^{-6}\,\text{m}^2\,\text{s}^{-1}$). For a screen of the size of a few tens of centimetres with a velocity of the order of 1 m s^{-1}, we obtain $Re \approx O(10^4) \gg 1$. We perform measurements with screens of different solidities, as well as made of different fibre radii and pore sizes while keeping the solidity almost constant, which allows us to probe the local effect of viscosity. The details of the wind tunnel as well as the characteristics of the flow can be found in the thesis of Du Pontavice (2016). The system is placed at a distance of approximately 50 cm from the outlet of the wind tunnel in order to obtain a free flow. Temperature and humidity were taken either from meteorological data of the site or local instruments placed upstream to reduce some of the uncertainty in the air density value. All the uncertainty estimates can be found in Appendix C. To compute the drag coefficient at normal incidence, 12 different velocities have been used as shown in figure 2(*a*) where we plotted the force as a function of velocity for several screens. From the force curves, we

Screen no.	Solidity s	Re_d	C_D	R^2	Screen no.	Solidity s	Re_d	C_D	R^2
P1	0.58	93–242	0.872	0.9995			39	0.205	
		354	0.625				46	0.186	
		422	0.608				54	0.176	
		494	0.604				62	0.169	
		565	0.607		P27	0.115	69	0.163	0.9125
P2	0.41	633	0.567	0.9977			77	0.158	
		704	0.568				85	0.155	
		776	0.573				93	0.156	
		848	0.559				100	0.154	
		915	0.552				142	0.148	
P3	0.87	609–1583	0.957	0.9998			169	0.146	
P4	0.61	83–217	0.922	0.9997			197	0.136	
P5	0.56	32–83	0.941	0.9995			226	0.139	
P6	0.61	58–150	0.935	0.9996	P28	0.114	253	0.139	0.9972
P7	0.45	87–225	0.705	0.9993			282	0.139	
P8	0.70	42–108	0.986	0.9992			310	0.136	
P9	0.26	2–5	0.976	0.9998			339	0.132	
P10	0.11	87–225	0.146	0.9990			366	0.129	
P11	0.37	87–225	0.596	0.9990			6	0.322	
		87	0.499				8	0.287	
		104	0.489				9	0.267	
		121	0.463				10	0.263	
		139	0.465		P29	0.080	12	0.245	0.7498
P12	0.31	155	0.459	0.9972			13	0.240	
		173	0.460				14	0.235	
		191	0.469				15	0.219	
		208	0.450				17	0.205	
		225	0.436				142	0.088	
P13	0.17	87–225	0.210	0.9988			169	0.085	
P14	0.24	87–225	0.328	0.9990			197	0.088	
P15	0.24	87–225	0.336	0.9994			226	0.092	
P16	0.24	87–225	0.343	0.9996	P30	0.080	253	0.087	0.9945
P17	0.15	87-225	0.198	0.9982			282	0.086	
P18	0.28	87–225	0.358	0.9983			310	0.080	
P19	0.52	83–217	0.803	0.9997			339	0.083	
P20	0.42	83–217	0.632	0.9995			366	0.079	
P21	0.32	83–217	0.406	0.9986	P31	1.00	—	0.939	0.9994
P22	0.65	16–42	0.956	0.9999					
P23	0.82	8–21	0.951	0.9998					
P24	0.75	10–25	0.960	0.9999					
P25	0.70	12–31	0.985	0.9998					
		142	0.623						
		169	0.610						
		197	0.583						
		226	0.584						
P26	0.405	253	0.594	0.9971					
		282	0.574						
		310	0.559						
		339	0.552						
		366	0.544						

Table 1. Porous screen characteristics. The interval of the Reynolds number Re_d is calculated with the fibre diameter d as characteristic size, with a velocity $v_0 = 5.0\,\mathrm{m\,s^{-1}}$ for the minimum value, a velocity $v_0 = 13.0\,\mathrm{m\,s^{-1}}$ for the maximum value and a kinematic viscosity $\nu = 15.6 \times 10^{-6}\,\mathrm{m^2\,s^{-1}}$. For the screens P2, P12, P26, P27, P28 P29 and P30, we put the detailed values of the drag coefficient at each velocity (and calculated the corresponding Reynolds number Re_d). The uncertainties as well as the fibre diameters, material type and geometry can be found in the Appendix C.

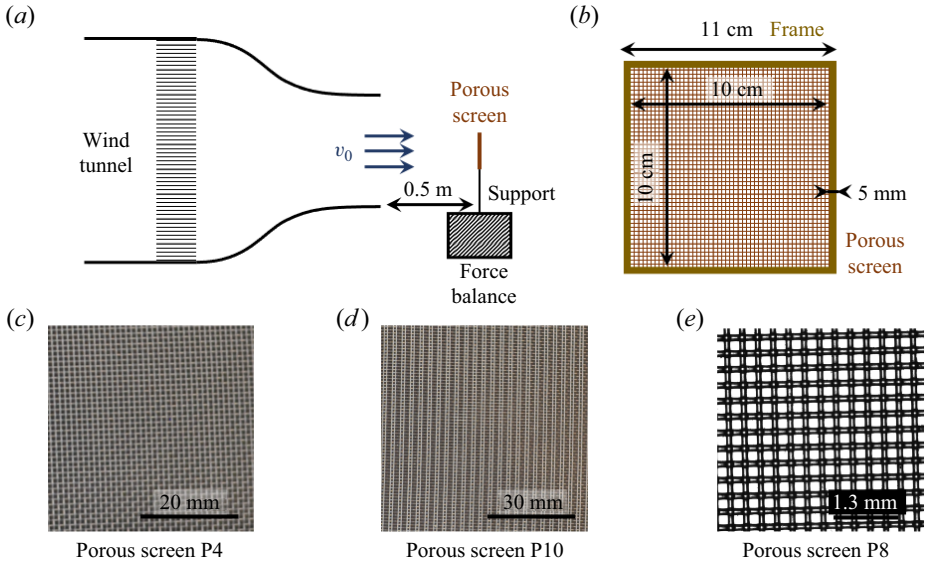

Figure 1. Diagram of the experimental set-up for the drag coefficient measurement, and examples of porous screens essentially in nylon woven mesh.

can then deduce a drag coefficient C_D defined as

$$C_D = \frac{F_D}{\frac{1}{2}\rho v_0^2 S_p}, \tag{2.2}$$

where ρ is the fluid (air) density and S_p the surface area of the screen. We note that here the surface S_p is the total surface area of the screen and not its projected area along the far-field stream direction $\boldsymbol{v_0}$. Figure 2(*b*) shows the measured drag coefficient C_D as a function of the velocity v_0 for different screens with different solidities s and fibre diameter d, after subtraction of the contribution of the frame and the mast detailed in Appendix C, and rescaled by the value at the largest velocity of the wind tunnel $C_D(v_{0_{max}})$. In most experiments, the drag coefficient does almost not vary with the incoming fluid velocity, i.e. the drag force is proportional to the square of the fluid velocity v_0 upstream from the screen. This is consistent with the fact that the Reynolds number is always high in our experiments ($32\,000 < Re < 83\,000$). However, we observe that for small fibre radii and low solidities, the drag coefficient decreases with increasing velocity, suggesting viscous effects. At higher velocity, the drag coefficient tends toward a constant. For screens that show almost constant value of the drag coefficient with respect to the velocity, the data can then be fitted with a quadratic law to obtain the drag coefficient C_D. We calculated the coefficient of determination R^2 associated to the fitting in table 1. For these screens, with almost constant drag coefficient, we always have $R^2 \geq 0.998$. For screens that show more important variation of the drag coefficient, we keep the value of the drag of each velocity between 5.0 and 13.0 m s^{-1}. Those values are reported in table 1. For comparison, we also calculated the coefficient of determination R^2 as if they were fitted by a quadratic law.

Figure 3 shows the characteristic drag coefficient of the square screens as a function of the solidity s. The drag coefficient increases with increasing solidity, until it reaches a constant value $C_D \simeq 1$ at high solidities (for $s \leq 0.7$). This evolution of the drag coefficient is qualitatively consistent with previous experiments in particular Prandtl & Flachsbart

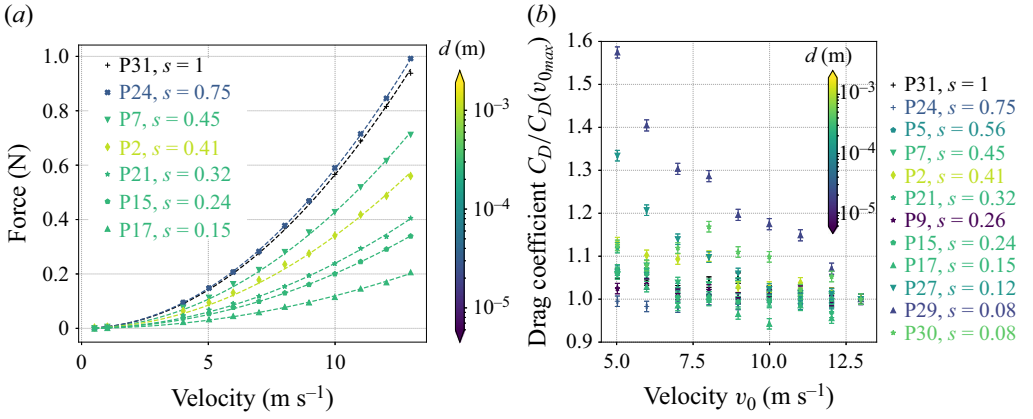

Figure 2. (*a*) Drag force (F_D) measured for different square porous screens at normal incidence. (*b*) Drag coefficient C_D as a function of velocity v_0, renormalised by the drag coefficient at maximum velocity for each screen $C_D(v_{0_{max}})$, including screens showing the higher variation of the drag coefficient with respect to the velocity. Colour bars: fibre diameter d.

(1932), as well as with the 2-D model derived by Steiros & Hultmark (2018). Furthermore, we observe that for a given solidity, the drag coefficient increases for decreasing d; this effect is particularly important at small solidities. In order to take into account the effect of the fibre diameter d, we define a local Reynolds number for the flow around each fibre denoted Re_d, for each screen, following

$$Re_d = \frac{v_0 d}{\nu} \tag{2.3}$$

as done in Prandtl & Flachsbart (1932). At moderately high Re_d ($\sim 10^2$), where viscous effects should not dominate the flow through the screen, the 2-D model overestimates the drag coefficient obtained experimentally, in particular at high solidities. This highlights the importance to take into account 3-D effects. At low Re_d, the model underestimates the drag coefficient, i.e. viscous effects must be included. We note that the model assumes a steady wake, and thus, is not applicable in the presence of vortex shedding. However, our experiments suggest that vortex shedding is negligible for our range of parameters, as further discussed in § 5.3.

To characterize the influence of the solidity on the flow deviation, we measure the flow field with a PIV method. We use a wind tunnel with square test section of width 22 cm at constant velocity $2.84 \pm 0.02\,\mathrm{m\,s^{-1}}$. The fluid is seeded with micro-droplets of water of diameter $3.0 \pm 2.0\,\mu\mathrm{m}$. The Stokes number is defined as

$$St = \frac{1}{18}\frac{\rho_p d_p^2 v_0}{\mu L_0}, \tag{2.4}$$

where ρ_p and v_p are the particles density and diameter, respectively, and $\mu = \rho\nu$ is the viscosity of the fluid. The Stokes number is of the order of $10^{-3} \ll 1$ and we can consider that the water droplets act as passive tracers of the flow. A 1 mm-thick laser sheet is used to highlight the particles in a plane parallel to the flow. The laser (Elforlight LTD.model FCHPG-3000) has a wavelength of 532 nm and maximum power of 6.0 W. A high-speed camera PHOTRON was used at a frame rate of 4000 fps to record successive images that have been analysed with PIVlab in MATLAB (version 2.62).

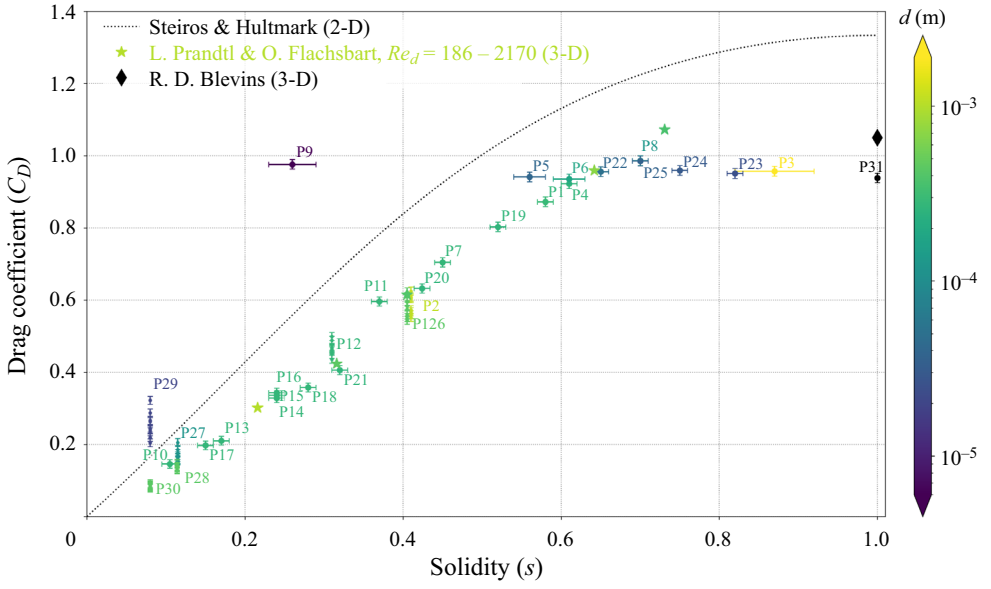

Figure 3. Drag coefficient $C_{D_{max}}$ as a function of the solidity for various square porous screens normal to the free flow and comparison with the 2-D model of Steiros & Hultmark (2018). The colour of the points indicates the value of the fibre diameter d following the colour scale on the right. The data from Prandtl & Flachsbart (1932) and the value at solidity $s = 1$ from Blevins (1992) are also plotted.

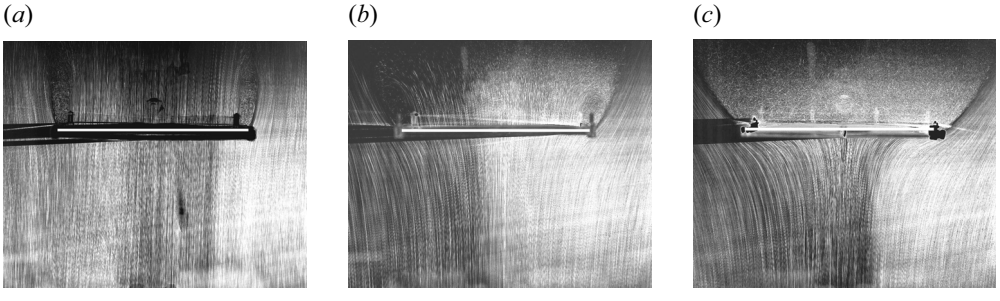

Figure 4. Experimental evidence of the deviation of the flow and streamlines around a square porous screen at different solidities s under normal uniform upstream flow $v_0 = 2.84 \pm 0.02\,\mathrm{m\,s^{-1}}$. Top view of the screen. The white bar (110 mm) corresponds to the screen embedded in the frame, the screen alone is 100 mm long. Results are shown for (*a*) P14, $s = 0.24$; (*b*) P6, $s = 0.61$; (*c*) P23, $s = 0.82$.

In figure 4 we show the trajectories of the particles in a plane orthogonal to the screen at mid-height (i.e. at the middle of the screen), obtained by the superposition of the maximum intensity of 2000 successive images. The upstream region is at the bottom of the figures and the downstream region at the top. We observe that the flow deviation around the screen increases as the solidity increases. We can further observe that the velocity decreases as the solidity increases, as shown by the variation of the length of the bright lines, shorter in figure 4(*b*) than in 4(*a*). Furthermore, in figure 4(*c*) we barely observe any particles crossing the screen, while some particles appear to be mixed by the recirculation in the wake.

In the following, we aim at developing a model that takes into account both 3-D and viscous effects. We then use this model to describe the flow around rectangular screens

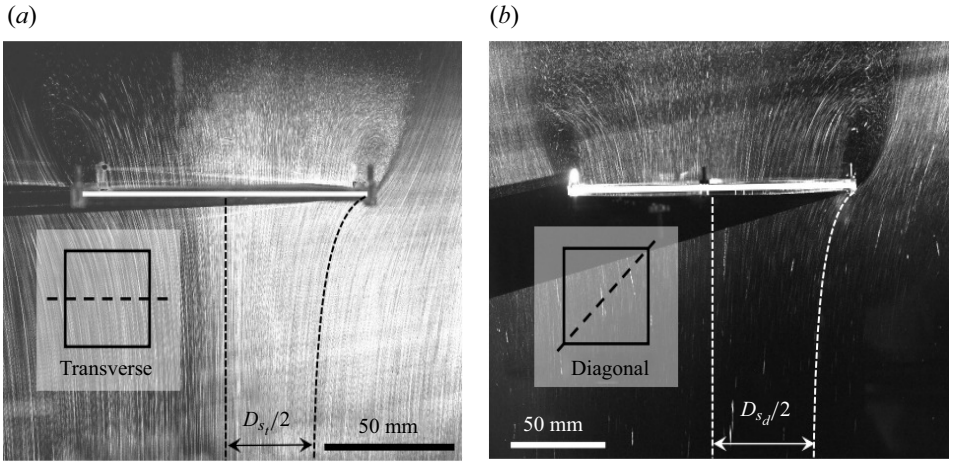

Figure 5. Experimental evidence of the 3-D deviation of the flow and streamlines around a square porous screen (transverse and diagonal directions) for a screen of solidity $s = 0.61$ (P6) under normal uniform upstream flow $v_0 = 2.84 \pm 0.02\,\mathrm{m\,s^{-1}}$. Here $D_{sd}/2 = 55.8 \pm 1.5\,\mathrm{mm}$ and $D_{st}/2 = 32.8 \pm 1.2\,\mathrm{mm}$; thus, $D_{sd}/D_{st} = 1.7 \pm 0.1 > \sqrt{2}$.

and predict the corresponding drag coefficient. In order to model these effects, we start by extending the 2-D model first proposed by Koo & James (1973) to a 3-D free flow and arbitrary shape, taking into account the base suction effect considered by Steiros & Hultmark (2018). We then derive the equations to predict the drag coefficient following the method proposed by Steiros & Hultmark (2018), and discuss the limits of this approach. In particular, while this approach takes into account some viscous effects in the pressure jump, it fails to describe the dependency of our measurements on Re_d. We thus incorporate in the model an empirical law as proposed by Brundrett (1993) for the pressure jump. Our modelling approach is sketched in figure 6.

In addition to these 2-D deviations, we observe 3-D deviations. In order to quantify them, we look at a plane in the diagonal direction (figure 5). In both the transverse and diagonal plane, we measure the proportion of deviated streamlines (i.e. the position of the separation distances D_{sd} and D_{st}). If the deviations were purely two dimensional, we would have $D_{sd} = \sqrt{2}D_{st}$, i.e. the streamtube formed by the separatrix would be square like the screens. If 3-D deviations occurs, the streamtube should be deformed, and, in particular, $D_{sd} > D_{st}$. In our experiments, we found that indeed $D_{sd}/D_{st} = 1.7 \pm 0.1 > \sqrt{2}$.

3. Three-dimensional model

In this section we derive the equations describing the 3-D flow around and through a porous screen with arbitrary shape and solidity. First, we adopt the method used by Koo & James (1973) that showed a good agreement with experimental results for 2-D flow in a channel except at high solidity. This discrepancy at high solidity may come from the lack of base pressure and vortex shedding in their theory, as suggested by Steiros & Hultmark (2018) (see §§ 3.4 and 3.5). We extend the model to the 3-D case for free flow, i.e. a case where there are no boundaries constraining the flow, which is one of the major differences with the model of Koo & James (1973). We also take into account the effect of the base pressure. We first obtain a general formulation of the equations for a porous screen of

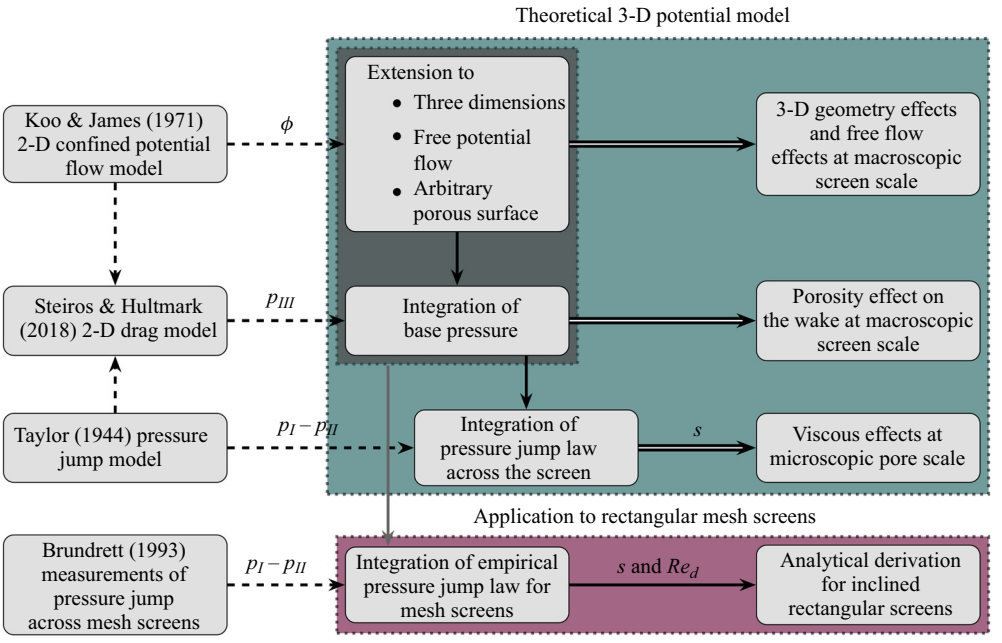

Figure 6. Diagram of the theoretical model derived in this study and the ingredients from previous models used. In blue, a complete 3-D potential model. In grey, the theoretical basis used for the application to rectangular mesh screens. In purple, the application to rectangular mesh screens. Here ϕ denotes the velocity potential, p_{III} denotes the base pressure and p_I–p_{II} denotes the pressure jump across the screen.

arbitrary shape. We then apply our equations to the case of a rectangular plate inclined in a laminar flow for which an analytical solution can be found.

3.1. *General formulation*

The flow around bluff bodies is complex. In order to obtain an analytical or semi-analytical description of the flow, a widely used approach consists in simplifying the governing equations using potential flow theory outside the wake while introducing free parameters such as base pressure to account for viscous and complex phenomena in the wake and near the solid structure (Parkinson & Jandali 1970). The model proceeds with the same idea. The system is separated into four regions delimiting four flow regimes, as shown in figure 7. The flow is assumed to be stationary, incompressible and inviscid everywhere except through the porous structure where viscous effects cannot be neglected.

In region I we assume that the flow is potential and the velocity is denoted $\boldsymbol{v}_I(x, y, z)$. Region I is located upstream of the structure as well as downstream outside the wake zone contained by a well-defined streamtube attached to the contour of the porous surface as shown in figure 7. Therefore, the velocity derives from a velocity potential denoted $\phi_I(x, y, z)$ for region I. Using the method employed by Koo & James (1973), and initially suggested by Taylor (1944), we calculate the flow by modelling the screen with a continuous source distribution with strength $\Omega(x_s, y_s, z_s)$, where (x_s, y_s, z_s) denotes a point on the surface. We obtain the potential flow in region I by superposing the resulting potential flow from the distribution of sources with the uniform laminar flow $\boldsymbol{v}_0$. The two streamfunctions ψ_I and χ_I needed to describe general 3-D incompressible flows can then be deduced using the following relation (for a definition of 3-D streamfunctions,

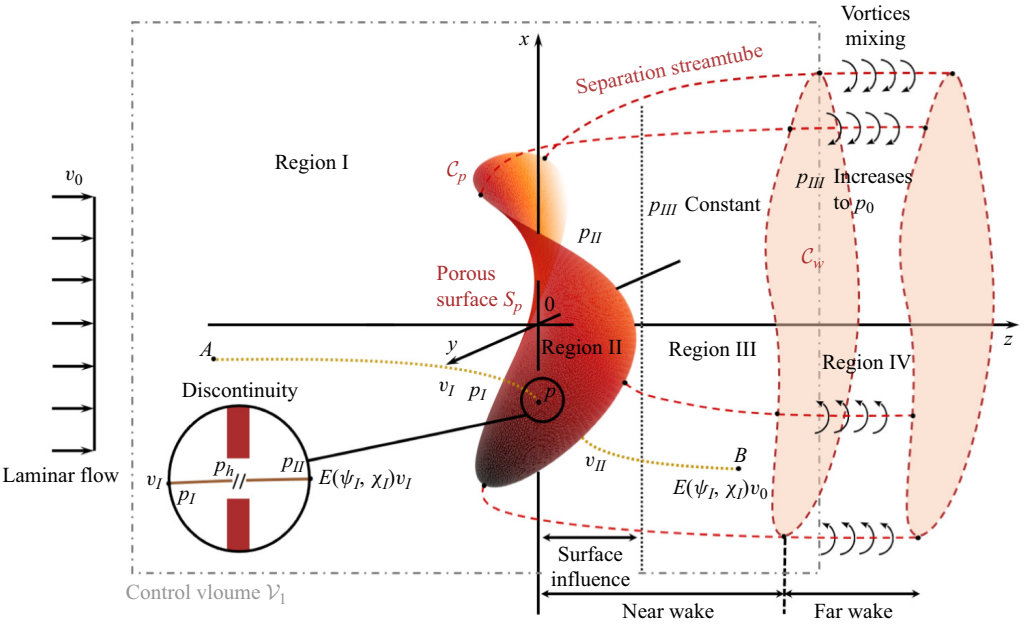

Figure 7. Diagram of the model for a 3-D potential flow around and through a porous screen. The dashed lines are the separation streamlines used as a boundary between the regions. The dotted lines are the streamlines used in the model to calculate the velocities in regions I and II. The incoming flow is laminar and is extended over the entire height of the system. Here $\mathcal{C}_w$ denotes the section of the wake.

see Yih 1957):

$$\boldsymbol{v}_I(x, y, z) = \nabla\psi_I(x, y, z) \wedge \nabla\chi_I(x, y, z). \tag{3.1}$$

Regions II and III are located downstream of the porous surface in the near wake. In these regions the flow can be rotational so that we cannot use anymore a velocity potential to describe the flow. In region II the pressure and the velocity are not constant since they are influenced by the surface. However, in region III the flow is sufficiently far from the screen so that the streamlines tend to be aligned with the uniform flow $\boldsymbol{v}_0$ as represented by the contour $\mathcal{C}_w$ in figure 7. Therefore, the pressure tends towards a base suction pressure p_{III} that is *a priori* different (and lower) than the constant external pressure p_0. This region is mathematically at infinity (there are no finite separations between regions II and III), however, since the flow aligns rapidly with the uniform flow, we indicate a region III in the near wake in figure 7. In two dimensions, the approach of constant pressure along separating streamlines has been successfully used in free-streamline theory by Wu (1962), Parkinson & Jandali (1970) and Roshko (1954) to model the wake. In this model, since we consider three dimensions, we can not adopt free-streamline theory, but p_{III} can be considered as having the same role as the constant pressure used in such theory. The flow in regions II and III is found with matching conditions as explained later.

In figure 7 we added a region IV that is located in the far wake where the mixing with the outer flow can not be ignored. In this region, the pressure should increase to reach again the pressure p_0 outside the wake. We assume that this region has little influence on the flow near the porous screen and on the aerodynamic forces, and therefore, it is not included in the model. Consequently, in our model the pressure in the far wake will remain equal to p_{III}.

3.2. *Determination of the flow in region I*

In region I the flow is potential, and we derive the velocity from the velocity potential. For simplicity, we set the reference frame so that the axis (Oz) is aligned with the velocity $\boldsymbol{v}_0$ without loss of generality. Due to the linearity of the Laplacian, we first consider the potential flow $\phi(x, y, z)$ for the source distribution only, then we add the potential flow for the uniform flow. The velocity potential from the source distribution Ω located on a general regular surface $\mathcal{S}_p$ is the solution of the equation

$$\Delta\phi(x, y, z) = \Omega(x, y, z)\mathbb{1}_{\mathcal{S}_p}, \tag{3.2}$$

where $\mathbb{1}_{\mathcal{S}_p}$ denotes the Dirac function associated to the surface $\mathcal{S}_p$. For a point source in three dimensions centred at the origin, the Green function of the Laplacian is

$$\Gamma(x, y, z) = -\frac{1}{4\pi}\frac{1}{\sqrt{x^2 + y^2 + z^2}}. \tag{3.3}$$

Therefore, if we assume $\boldsymbol{\xi} : U \subset \mathbb{R}^2 \to \mathbb{R}^3$ to be a surface patch of a general regular surface $\mathcal{S}_p$ with coordinates

$$\boldsymbol{\xi} = \begin{pmatrix} x_s(u, v) \\ y_s(u, v) \\ z_s(u, v) \end{pmatrix}, \tag{3.4}$$

parametrized by two parameters u and v, with $(u, v) \in (U = [a, b] \times [c, d])$ with $(a, b, c, d) \in \mathbb{R}^4$, then the velocity potential $\phi(x, y, z)$ is expressed for all $(x, y, z) \in \mathbb{R}^3 \setminus \mathcal{S}_p$ as (Pressley 2010)

$$\phi(x, y, z) = \iint_U \Omega(u, v)\Gamma(x - x_s(u, v), y - y_s(u, v), z - z_s(u, v)) \left\| \frac{\partial\boldsymbol{\xi}}{\partial u} \wedge \frac{\partial\boldsymbol{\xi}}{\partial v} \right\| \mathrm{d}u\,\mathrm{d}v, \tag{3.5}$$

and the total velocity potential can be written as the sum

$$\phi_I(x, y, z) = v_0 z + \phi(x, y, z). \tag{3.6}$$

We deduce the velocity in region I with $\boldsymbol{v_I}(x, y, z) = \boldsymbol{grad}(\phi_I(x, y, z))$. Note that the Green function can be changed without other modifications in the model to study the situation of a flow in a confined environment or near a wall.

3.3. *Determination of the flow in regions II and III*

In region II the flow can be rotational, and therefore, is not necessarily potential. The flow is obtained from the streamfunctions by considering, as done by Koo & James (1973), that the streamlines in region II have the same pattern as if they were obtained by the streamfunctions from the superposition of the distribution of sources and the uniform flow $\boldsymbol{v}_0$. This can be formulated in a general way by writing the two streamfunctions for the flow in region II as functions of the streamfunctions of region I. Let ψ_{II} and χ_{II} be the streamfunctions in region II. As defined above, ψ_I and χ_I are the streamfunctions deduced from the flow in region I, functions that can be considered in the whole space. Then, without loss of generality, we choose an analog formulation as the one

proposed by Koo & James (1973) to describe the flow in region II, using the functions f and g:

$$\psi_{II} = f(\psi_I)\psi_I \quad \text{and} \quad \chi_{II} = g(\chi_I)\chi_I. \tag{3.7a,b}$$

This means that the velocity $\boldsymbol{v}_{II}$ in region II, and the velocity $\boldsymbol{v}_I$ obtained from the velocity potential $\phi_I(x, y, z)$, are co-linear at any point. We indeed obtain

$$\boldsymbol{v}_{II}(x, y, z) = \left(\frac{\mathrm{d}f}{\mathrm{d}\psi_I} + f(\psi_I)\right)\left(\frac{\mathrm{d}g}{\mathrm{d}\chi_I} + g(\chi_I)\right)\boldsymbol{v}_I(x, y, z). \tag{3.8}$$

We define the attenuation function E as

$$E(\psi_I, \chi_I) = \left(\frac{\mathrm{d}f}{\mathrm{d}\psi_I} + f(\psi_I)\right)\left(\frac{\mathrm{d}g}{\mathrm{d}\chi_I} + g(\chi_I)\right), \tag{3.9}$$

which is the crucial quantity to determine the flow in region II. Since E is a function only of the streamfunctions, it is constant along a streamline and is therefore entirely defined by considering its value on the screen.

In addition to (3.8), the mass flow rate must be conserved when the fluid passes through the screen implying the continuity of the normal velocity at the screen between region I and region II:

$$v_{In}(x_s, y_s, z_s) = v_{IIn}(x_s, y_s, z_s). \tag{3.10}$$

At this point, our system thus contains two unknowns that are the attenuation function E and the distribution of sources Ω. We have one equation (3.10), and another equation linking the velocities and pressures in the vicinity of the porous structure is required to close our system of equations. For this purpose, two streamlines are considered as shown in figure 7: (AP) and (PB) where the point P is on the screen taken as a surface from a macroscopic point of view. Along each of these streamlines, Bernoulli's equation can be applied, and we thus obtain, for (AP),

$$\tfrac{1}{2}\rho v_I^2(x_A, y_A, z_A) + p_I(x_A, y_A, z_A) = \tfrac{1}{2}\rho v_I^2(x_s, y_s, z_s) + p_I(x_s, y_s, z_s), \tag{3.11}$$

and, for (PB),

$$\tfrac{1}{2}\rho v_{II}^2(x_s, y_s, z_s) + p_{II}(x_s, y_s, z_s) = \tfrac{1}{2}\rho v_{II}^2(x_B, y_B, z_B) + p_{II}(x_B, y_B, z_B). \tag{3.12}$$

We consider that the points A and B are far enough from the screen so that we can take constant values of the velocities and pressures (see Fail, Lawford & Eyre (1957) for flat plates normal to an air stream). Therefore, upstream we have $\boldsymbol{v}_I(x_A, y_A, z_A) = \boldsymbol{v}_0$ and $p_I(x_A, y_A, z_A) = p_0$; downstream we take the mean value of the velocity over a section of the wake orthogonal to the far-field stream direction $(\boldsymbol{v}_0)$: $\boldsymbol{v}_{II}(x_B, y_B, z_B) = \overline{\lim_{z\to+\infty} \boldsymbol{v}_{II}(x, y, z)} = \overline{E(\psi_I, \chi_I)}\boldsymbol{v}_0$. In the rest of the paper, $\overline{E(\psi_I, \chi_I)}$ will be denoted as $\overline{E}$. Koo & James (1973) considered a far-downstream constant pressure p_0; however, it is known that the pressure in the wake is lower than the pressure outside the wake that contributes to aerodynamic forces. Steiros & Hultmark (2018) therefore introduced a suction base pressure p_{III} at the point B, which is assumed to be constant far enough from the screen in region III as explained above. Thus, we introduce a third free parameter p_{III} that will be determined from conservation equations in § 3.5. Note that since we

assume that the pressure p_{III} is constant, the pressure will be discontinuous across the wake boundaries (as in the model of Koo & James (1973) in the 2-D case). By combining (3.11) and (3.12), decomposing the velocities according the tangential and normal components on the screen (respectively, v_{It} and v_{In}) and by using (3.10), we obtain the pressure difference

$$p_0 - p_{III} = \tfrac{1}{2}\rho(1 - E^2(\psi_I, \chi_I))v_{It}^2(x_s, y_s, z_s) + \tfrac{1}{2}\rho(\bar{E}^2 - 1)v_0^2 + p_I(x_s, y_s, z_s) - p_{II}(x_s, y_s, z_s). \tag{3.13}$$

If we are able to determine the pressure differences $p_0 - p_{III}$ and $p_I(x_s, y_s, z_s) - p_{II}(x_s, y_s, z_s)$ independently from these equations, then we can use (3.10) to find the attenuation function E and (3.13) to find the distribution of sources Ω. In order to determine the suction pressure p_{III}, we follow the method of Steiros & Hultmark (2018) in § 3.5, using the conservation law of the momentum in the control volume V_1 shown in figure 7, and at the vicinity of the screen. Before addressing this problem, we focus in the following § 3.4 on the pressure jump $p_I(x_s, y_s, z_s) - p_{II}(x_s, y_s, z_s)$.

3.4. *Pressure jump across the screen*

A summary of the models for the relation between the pressure jump and screen porosity can be found in Xu *et al.* (2020). This problem has largely been discussed in many papers, raising the difficulties of a general formulation. In their model, Steiros & Hultmark (2018) consider two streamlines passing through the screen in a hole where the velocity and the pressure are assumed to be uniform. Immediately upstream after the acceleration of the fluid, the characteristic pressure of the flow is denoted p_h and is assumed to correspond physically to the mean pressure inside the hole. As noted by several authors including Taylor & Davies (1944) and Wieghardt (1953), the characteristic velocity immediately upstream should be regarded as the mean velocity after contraction of the flow within the holes, v_{h1}, denoting the average velocity through the screen expressed as

$$v_{h1} = \frac{v_{In}(x_s, y_s, z_s)}{(1 - s)}, \tag{3.14}$$

The velocity accelerates to v_{h1} in the hole and the pressure decreases to p_h so that at this point there are no losses. Along this first streamline, Bernoulli's equation leads to

$$p_I(x_s, y_s, z_s) + \tfrac{1}{2}\rho v_I^2(x_s, y_s, z_s) = p_h + \tfrac{1}{2}\rho v_{h1}^2. \tag{3.15}$$

Immediately downstream, considering also a homogenized velocity, the flow enlarges and the velocity reaches a value equal to

$$v_{h2} = v_{IIn}(x_s, y_s, z_s), \tag{3.16}$$

taken as the characteristic velocity just after the hole. As discussed by Taylor & Davies (1944) and Steiros & Hultmark (2018), there are pressure losses in the pores, i.e. $p_{II} < p_I$. Taylor & Davies (1944) consider that a fraction λ of the pressure lost in acquiring the velocity v_h is regained when the stream becomes uniform again behind the sheet. Steiros & Hultmark (2018) consider that the pressure loss during the fluid acceleration is not recovered, i.e. all surplus kinetic energy due to fluid acceleration is lost and not reconverted

into pressure (i.e. $\lambda = 0$). In that case, Bernoulli's equation along this second streamline leads to

$$p_h + \tfrac{1}{2}\rho v_{h2}^2 = p_{II}(x_s, y_s, z_s) + \tfrac{1}{2}\rho v_{II}^2(x_s, y_s, z_s). \tag{3.17}$$

We combine (3.8), (3.10) and (3.14)–(3.17) to obtain

$$\begin{aligned} p_{II}(x_s, y_s, z_s) - p_I(x_s, y_s, z_s) = {} & \tfrac{1}{2}\rho v_{I_t}^2(x_s, y_s, z_s)(1 - E^2(\psi_I, \chi_I)) \\ & + \tfrac{1}{2}\rho v_{I_n}^2(x_s, y_s, z_s)\theta(s), \end{aligned} \tag{3.18}$$

with

$$\theta(s) = 1 - \frac{1}{(1-s)^2}. \tag{3.19}$$

Injecting the pressure difference p_I–p_{II} obtained in (3.18) in (3.13), we have

$$p_0\text{–}p_{III} = -\tfrac{1}{2}\rho v_{I\,n}^2(x_s, y_s, z_s)\theta(s) + \tfrac{1}{2}\rho(\bar{E}^2 - 1)v_0^2. \tag{3.20}$$

We assumed that p_{III} is constant, therefore, the right-hand side of the above equation has to be constant, which leads to the condition

$$\boldsymbol{grad}_{\mathcal{S}_p}(v_{I_n}^2(x_s, y_s, z_s)\theta(s)) = \boldsymbol{0}, \tag{3.21}$$

with $\theta(s)$ that can vary for non-homogeneous porous surfaces. Therefore, under the assumptions made so far, we are looking for a source strength Ω that satisfies this condition. It is possible to relax certain restrictions on the value of Ω by considering a variable base suction pressure p_{III} or a variable far wake velocity $\boldsymbol{v}_{II}(x_B, y_B, z_B) = E(\psi_I, \chi_I)\boldsymbol{v}_0$. In that case, the problem is far more difficult, and should be solved numerically. Such a resolution is beyond the scope of the present work.

3.5. *Drag coefficient*

At this point, our system of equations is not closed. Therefore, in this section we find another equation by adapting the model of Steiros & Hultmark (2018) in three dimensions with a screen of arbitrary shape and orientation in the flow. It uses two expressions of the aerodynamic forces that can be combined to give a final equation, closing eventually our system of equations.

A first expression is given by the momentum balance around the surface of the screen, using the drag coefficient as defined in (2.2), giving

$$C_D = \frac{1}{\frac{1}{2}\rho S_p v_0^2}\left(\iint_{\mathcal{S}_p}(p_I\text{–}p_{II})\boldsymbol{e}_z \cdot \boldsymbol{n}_s \,\mathrm{d}S + \rho \iint_{\mathcal{S}_p} v_{In}\boldsymbol{e}_z \cdot (\boldsymbol{v}_I\text{–}\boldsymbol{v}_{II})\,\mathrm{d}S\right), \tag{3.22}$$

where the normal vector $\boldsymbol{n}_s$ points in the direction of region II. The pressure difference p_I–p_{II} in (3.22) is given by (3.18).

The second expression of the drag coefficient is provided by the momentum balance in a control volume V_1 around the screen as shown in figure 7. We consider that this volume V_1 is large enough so that the velocities at the surfaces $\mathcal{S}_x$ and $\mathcal{S}_y$ on the sides of the block parallel to the z axis are equal to $\boldsymbol{v}_0 + \boldsymbol{v}_\epsilon$ where $v_\epsilon \ll v_0$. With this approximation, the

projection of momentum balance equation onto the far-field stream direction ($\boldsymbol{v}_0$) gives an expression of the drag F_D,

$$F_D = \rho S_w(1-\bar{E}^2)v_0^2 + S_w(p_0{-}p_{III}) - \rho v_0 \iint_{\mathcal{S}_x+\mathcal{S}_y} \boldsymbol{v}_I \cdot \boldsymbol{n}\,\mathrm{d}S, \tag{3.23}$$

where S_w is the area of the section of the wake (orthogonal to the z axis), and the bar over E denotes the mean over the considered surface. The normal vector $\boldsymbol{n}$ points outwards from the control volume. Then, a mass balance in the same control volume gives

$$\rho v_0 S_w = \rho \iint_{\mathcal{S}_x+\mathcal{S}_y} \boldsymbol{v}_I \cdot \boldsymbol{n}\,\mathrm{d}S + \rho\bar{E}v_0 S_w. \tag{3.24}$$

This equation allows us to find the value of the last term of the conservation of momentum equation (3.23). Moreover, the section of the wake S_w is determined with a mass balance through the screen

$$\rho \iint_{\mathcal{S}_p} \boldsymbol{v}_I \cdot \boldsymbol{n}\,\mathrm{d}S = \rho\bar{E}v_0 S_w. \tag{3.25}$$

Equations (3.23)–(3.25) are now combined to obtain a second expression of the drag coefficient, which reads

$$C_D = \frac{1}{\frac{1}{2}\rho S_p v_0^2}(p_0{-}p_{III} + \rho v_0^2(\bar{E}-\bar{E}^2))\frac{1}{v_0\bar{E}}\iint_{\mathcal{S}_p} v_{I_n}\,\mathrm{d}S. \tag{3.26}$$

Equation (3.20) giving an expression of $p_0{-}p_{III}$ is used so that the second expression of the drag (3.26) is calculated further:

$$C_D = \frac{1}{S_p}(-(1-\bar{E})^2 - v_{I_n}^2\theta(s))\frac{1}{v_0\bar{E}}\iint_{\mathcal{S}_p} v_{I_n}\,\mathrm{d}S. \tag{3.27}$$

The final equation of the problem is obtained by equalizing the two expressions of the drag coefficient (3.22) and (3.27), yielding

$$\begin{aligned}\bar{E}\iint_{\mathcal{S}_p} (\tilde{v}_{I_t}^2(1-E^2) + \tilde{v}_{I_n}^2\theta(s))\boldsymbol{n}_s\cdot\boldsymbol{e}_z + 2\tilde{v}_{I_n}(1-E)\tilde{\boldsymbol{v}}_{I_t}\cdot\boldsymbol{e}_z\,\mathrm{d}S \\ = (-(1-\bar{E})^2 - \tilde{v}_{I_n}^2\theta(s))\iint_{\mathcal{S}_p}\tilde{v}_{I_n}\,\mathrm{d}S,\end{aligned} \tag{3.28}$$

with dimensionless velocities $\tilde{v} = v/v_0$.

Finally, we give the explicit expression for v_{I_n} and E. Finding v_{I_n} leads to a boundary surface potential problem. An explicit expression of v_{I_n} is found from the gradient of the velocity potential (3.6) having therefore an integral term. This integral term is known as a harmonic double-layer potential with density Ω (Gunter 1967), which is defined on a subdomain of $\mathbb{R}^3 \setminus \mathcal{S}_p$. This integral term becomes singular if it is evaluated on the surface $\mathcal{S}_p$, however, it can be continuously extended on the surface for each side and the value depends on the side by which we approach the surface. From the definitions of regions I

and II, for $\boldsymbol{m} = (x, y, z) \in \mathcal{S}_p$, we have

$$v_{I_n}(\boldsymbol{m}) = v_0 \boldsymbol{e_z} \cdot \boldsymbol{n}_s + v_n^-(\boldsymbol{m}), \tag{3.29}$$

and

$$v_{II_n}(\boldsymbol{m}) = E(\psi_I, \chi_I)(v_0 \boldsymbol{e_z} \cdot \boldsymbol{n}_s + v_n^+(\boldsymbol{m})), \tag{3.30}$$

with

$$v_n^{\pm}(\boldsymbol{m}) = \lim_{\epsilon \to 0^+} \frac{\partial \phi}{\partial \boldsymbol{n}_s}(\boldsymbol{m} \pm \epsilon \boldsymbol{n}_s), \tag{3.31}$$

with ϕ defined in (3.5) and the directional outward normal derivative

$$\frac{\partial \phi}{\partial \boldsymbol{n}_s}(\boldsymbol{m}) = \boldsymbol{grad}(\phi(\boldsymbol{m})) \cdot \boldsymbol{n}_s. \tag{3.32}$$

From a theorem that can be found, for instance, in Kress (1999, p. 80), the value of the limits above can be expressed using an improper integral. For $\boldsymbol{m} = (x, y, z) \in \mathcal{S}_p$, this expression reads

$$v_n^{\pm}(\boldsymbol{m}) = \iint_U \Omega(u, v) \frac{\partial \Gamma}{\partial \boldsymbol{n}_s}(\boldsymbol{m} - \boldsymbol{m}_s(u, v)) \left\| \frac{\partial \boldsymbol{\xi}}{\partial u} \wedge \frac{\partial \boldsymbol{\xi}}{\partial v} \right\| \mathrm{d}u \, \mathrm{d}v \pm \frac{1}{2} \Omega(\boldsymbol{m}), \tag{3.33}$$

with $\boldsymbol{m}_s(u, v) = (x_s(u, v), y_s(u, v), z_s(u, v))$. Finally, E is found by applying the continuity equation (3.10) for the normal velocities across the surface, with the expressions given in (3.29) and (3.30). For $\boldsymbol{m} = (x, y, z) \in \mathcal{S}_p$, we have

$$E(\boldsymbol{m}) = \frac{v_0 \boldsymbol{e_z} \cdot \boldsymbol{n}_s + v_n^-(\boldsymbol{m})}{v_0 \boldsymbol{e_z} \cdot \boldsymbol{n}_s + v_n^+(\boldsymbol{m})}. \tag{3.34}$$

The system of equations is now closed and enables us to obtain the velocities and pressure at any location in the flow by determining the source strength Ω, solution of (3.28). In the next section we solve the problem analytically in a basic but very common geometry.

3.6. *Application to an inclined rectangular screen in free flow*

For a rectangular geometry and homogeneous solidity, it is possible to obtain without major difficulty an analytical solution of the equations of our model. We therefore apply the 3-D model to the simple case of a rectangular screen (centred at $z = 0$ as shown in the figure 8) in a free laminar flow in order to find the flow and the drag coefficient as a function of the solidity. In that case, the velocity potential (3.6) becomes

$$\phi_I(x, y, z) = v_0 z + c - \frac{1}{4\pi} \iint_{\mathcal{S}_p} \frac{\Omega(u, v) \, \mathrm{d}u \, \mathrm{d}v}{\sqrt{(x - v)^2 + (y - u \sin(\beta))^2 + (z - u \cos(\beta))^2}}. \tag{3.35}$$

We then calculate the velocities at the screen. The objective of the calculus is to obtain Ω as a function of the solidity, which will determine all the other variables of the problem.

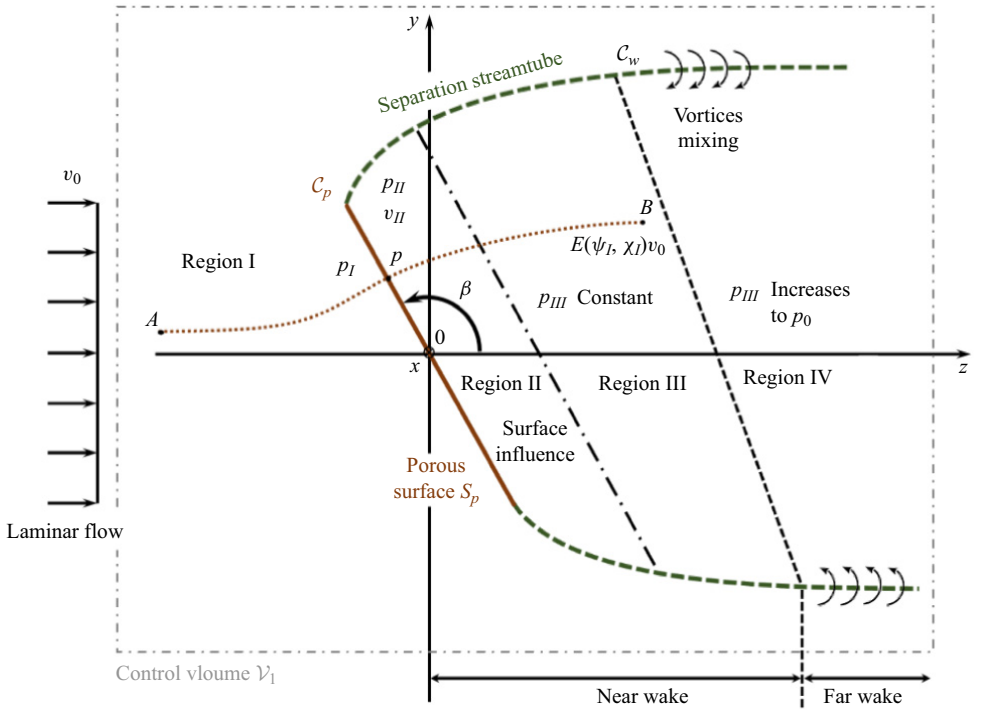

Figure 8. Diagram of the inclined rectangular porous screen in the (Oyz) plane in a 3-D free flow with an angle β. The dashed lines are the separation streamlines used as a boundary between the regions of the model. The dotted line between points A and B is the streamline used in the model to calculate the velocities in the regions I and III. The incoming flow is laminar.

The normal component of the velocity in region I at the arbitrary position (w, t) on the surface is

$$v_{I_n}^{\pm}(w,t) = v_0 \sin(\beta) + \lim_{\epsilon \to 0^{\pm}} \frac{1}{4\pi} \iint_{\mathcal{S}_p} f_\epsilon(u,v)\Omega(u,v)\,\mathrm{d}u\,\mathrm{d}v, \tag{3.36}$$

with

$$f_\epsilon(u,v) = \frac{\epsilon \cos(\beta)\sin(\beta)}{((t-v)^2 + (w-u)^2 + (2(w-u)+\epsilon)\epsilon\cos(\beta))^{3/2}}. \tag{3.37}$$

The details of the calculations are given in Appendix B. At the screen, depending on the direction from which we approach the screen ($\epsilon \to 0^{\pm}$), the magnitude of the normal component of the velocity is constant and is equal to

$$v_{In}(w,t) = v_n^-(w,t) = v_0 \sin(\beta) - \tfrac{1}{2}\Omega(w,t), \tag{3.38}$$

$$v_{IIn}(w,t) = E(\psi_I,\chi_I)v_n^+(w,t) = E(\psi_I,\chi_I)(v_0\sin(\beta) + \tfrac{1}{2}\Omega(w,t)). \tag{3.39}$$

At this point, for an homogeneous screen (s constant on the surface), (3.21) leads to $\boldsymbol{grad}(\Omega(w,t)) = \mathbf{0}$, i.e. the source strength is a constant.

Thus, (3.10) leads to a constant attenuation function

$$E = \frac{v_0 \sin(\beta) - \frac{1}{2}\Omega}{v_0 \sin(\beta) + \frac{1}{2}\Omega}. \tag{3.40}$$

If we found constant normal velocity, it is not the case of the tangential velocity for which the magnitude varies on the surface of the screen. The tangential component of the velocity at the surface is

$$\begin{aligned} v_{It}(x, w) = (&\Omega^2 \mathcal{I}_x^2(x, w) + (\Omega(\sin(\beta)\mathcal{I}_y(x, w) + \cos(\beta)\mathcal{I}_z(x, w)) \\ &+ \cos(\beta) v_0)^2)^{1/2}, \end{aligned} \tag{3.41}$$

with $\mathcal{I}_x$, $\mathcal{I}_y$ and $\mathcal{I}_z$ the following surface integrals that are calculated in Appendix A:

$$\mathcal{I}_x(x, w) = \frac{1}{4\pi} \iint_{\mathcal{S}_p} \frac{x - v}{((x - v)^2 + (w - u)^2)^{3/2}} \mathrm{d}u\, \mathrm{d}v, \tag{3.42}$$

$$\mathcal{I}_y(x, w) = \frac{1}{4\pi} \iint_{\mathcal{S}_p} \frac{(w - u)\sin(\beta)}{((x - v)^2 + (w - u)^2)^{3/2}} \mathrm{d}u\, \mathrm{d}v, \tag{3.43}$$

$$\mathcal{I}_z(x, w) = \frac{1}{4\pi} \iint_{\mathcal{S}_p} \frac{(w - u)\cos(\beta)}{((x - v)^2 + (w - u)^2)^{3/2}} \mathrm{d}u\, \mathrm{d}v. \tag{3.44}$$

For the sake of simplicity, we approximate the magnitude of the tangential component of the velocity as its root mean square. We note that since in (3.28), v_{I_t} appears both in linear and quadratic form, this approximation becomes exact for a surface normal to the mean flow direction ($\beta = \pi/2$). We thus take

$$v_{I_t} = (\Omega^2 \gamma_0 + v_0^2 \cos^2(\beta))^{1/2}, \tag{3.45}$$

where γ_0 can be considered as a shape factor (see Appendix A). Equation (3.18) becomes

$$p_{II} - p_I = \tfrac{1}{2}\rho(v_{I_t}^2(1 - E^2) + v_{I_n}^2\theta(s)). \tag{3.46}$$

Equation (3.13) leads to

$$\begin{aligned} p_{III} - p_0 &= \tfrac{1}{2}\rho(1 - E^2)(v_0^2 - v_{I_t}^2) + p_{II} - p_I \\ &= \tfrac{1}{2}\rho((1 - E^2)v_0^2 + v_{I_n}^2\theta(s)). \end{aligned} \tag{3.47}$$

Using (3.23)–(3.25), we obtain a first expression of the magnitude of the drag force F_D:

$$F_D = \rho v_0(1 - E)v_n S_p + \frac{1}{v_0}(p_0 - p_{III})\frac{v_n}{E} S_p. \tag{3.48}$$

The second expression for the drag force F_D is obtained with (3.22),

$$F_D = (p_I - p_{II})\sin(\beta) S_p + \rho v_n v_0 \cos^2(\beta)(1 - E) S_p. \tag{3.49}$$

Note that, for a rectangular screen orthogonal to the free flow, the second term of (3.49) vanishes since $\beta = \pi/2$ and we obtain a drag coefficient proportional to the pressure

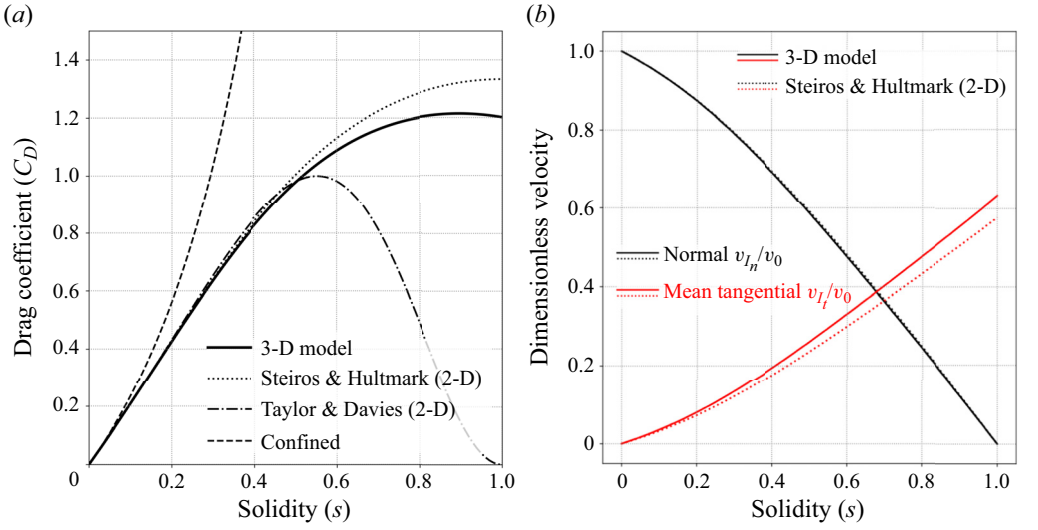

Figure 9. Theoretical prediction of the drag coefficient and velocities on the surface as a function of the solidity obtained with the 3-D model applied to a square homogeneous screen normal to the flow ($\beta = \pi/2$), and comparison with different 2-D models. The full lines are obtained with the 3-D model developed in this paper using the same pressure jump law across the screen as Steiros & Hultmark (2018) (but taking account of geometric 3-D effects). (*a*) Drag coefficient. (*b*) Normal velocity and quadratic mean of the tangential velocity as defined respectively in (3.38) and (3.45). (*a*) Theoretical drag coefficient. (*b*) Theoretical velocity at the screen.

difference p_I–p_{II}. Now, by denoting $\omega = \Omega/v_0$ and combining (3.48) and (3.49), we obtain the following equation that we have to solve to find the value of the source strength:

$$-\tfrac{1}{8}\omega^4\theta(s) + \omega^2\sin^2(\beta)(8\gamma_0 + \theta(s) - 2) - 4\omega\sin(\beta) - 2\sin^4(\beta)\theta(s) = 0. \quad (3.50)$$

This equation has been solved using Python 3.9.5 and the method fsolve from scipy.optimize. The solution for a square porous plate at normal incidence with $\beta = \pi/2$ is plotted in figure 9(*a*). At low solidity, our model for a square plate is close to the prediction of Steiros & Hultmark (2018) and Taylor & Davies (1944). Above a solidity $s = 0.4$ the drag coefficient becomes slightly different from the prediction of Steiros & Hultmark (2018) and the difference increases with increasing solidity. Three-dimensional effects are therefore important at high solidity.

At high solidity ($s \lesssim 1$), the curve converges towards the drag coefficient of a flat solid plate. This value is predicted to be 1.2 in our model, which is close to the experimental measurement at the global Reynolds number $Re \approx 10^4$, giving approximately 1.05 according to Blevins (1992), 1.17 according to the synthesis of Hoerner (1965) on various drag measurements and 0.939 in pour experiments.

Our model takes into account the shape of the porous surface through the parameter γ_0. For a rectangular screen, the aspect ratio, taken into account in γ_0, has an influence on the result as detailed in Appendix A. According to Hoerner (1965), for a flat plate normal to the flow, the drag coefficient increases very slowly when the aspect ratio is reduced until a ratio of approximately 0.1. Beyond this point the increase becomes more pronounced, until it reaches $C_D = 2.0$ for an infinitely thin plate (1.90 according to Blevins 1992). In our model, we indeed observe an increase of the drag when the aspect ratio decreases (see Appendix A) from $C_D = 1.2$ for a square plate (with $\gamma_0 = 0.0998$), 1.29 for a rectangle with aspect ratio 1/10 (with $\gamma_0 = 0884$) to $C_D = 1.33$ for an infinitely thin plate. This

value for an infinitely thin plate is lower than the experimental value, that is, $C_D \approx 2.0$ according to Blevins (1992) and Hoerner (1965). This difference may be due, in this case of very high aspect ratio, to the vortex shedding that is not taken into account in the present wake model, as noted by Steiros & Hultmark (2018).

In figure 9(*b*) we compare the normal and tangential velocities in the 2-D and 3-D cases. The tangential velocity is taken in both cases as the quadratic mean over the whole surface, in three dimensions it is defined in (3.45), the normal velocity is constant on the surface in both cases also, in three dimensions it is defined in (3.38). While the normal velocity is the same in two dimensions and three dimensions, we see an influence of 3-D effects on the tangential velocity.

While taking into account the 3-D effects improve the prediction of C_D at high solidities, it does not improve the prediction at moderate and low solidities. The limitations of potential flow theory to describe the complex flow around bluff bodies are arising at high solidity, but should be negligible at low and moderate solidity. Here, we hypothesize that the main reason for the discrepancy between our experimental results (figure 3) and the theoretical prediction (figure 9*a*) lies in the pressure loss at the pore scale. Indeed, the relation used to estimate the pressure jump p_I–p_{II} (3.18) is a strong assumption, and does not consider the pressure losses by viscous friction. In particular, it does not explicitly account for the viscosity, and can not account for the variations of the drag coefficient with the local Reynolds number observed in the experiments.

4. Local viscous effects

As we have seen, the pressure losses are accounted for in (3.18) with the parameter $\theta(s)$ given by (3.19). We have adopted the assumption of Steiros & Hultmark (2018), i.e. that all energy due to fluid acceleration is lost and not reconverted into pressure, which is a crucial assumption. The approach of Taylor & Davies (1944) is to assume that a fraction λ of energy is regained, which would modify $\theta(s)$ to read

$$\theta^*(s) = 1 - \frac{1-\lambda}{(1-s)^2}. \tag{4.1}$$

In their experiments, Taylor & Davies (1944) estimate $\lambda \simeq 0.4$. Taking into account this effect would decrease the drag coefficient, i.e. bring it closer to our experimental values at high Re_d. However, λ can only be obtained empirically. Furthermore, in our experiments, Re_d is smaller than the critical value of $\approx$1000 above which viscous effects can be neglected (Hoerner 1952). We thus want to account for the pressure losses due to viscous friction as well. One possible approach is to tune the pressure loss term in (3.18) with a single prefactor $\theta(s)f$ that should depend on Re_d; it should increase as Re_d decreases, accounting for increased viscous dissipation. This prefactor $\theta(s)f(Re_d)$ has been determined experimentally for wire screens by Brundrett (1993) and Bailey *et al.* (2003). In this section we follow their approach to include viscous effects and compare our predictions with experimental results.

4.1. *Pressure jump dependency on the local geometry of the pores and viscous effects*

As explained above, in the equation of the pressure jump (3.18) with (3.19), as formulated by Steiros & Hultmark (2018), we do not take into account the dependency of the pressure drop on the local Reynolds number Re_d, computed at the scale of the screen pores (and thus, much smaller than Re), the geometry of the holes and other possible dependency

like the energy transfer between the material of the screen and the fluid. For instance, Ando *et al.* (2022) showed that a layer of flexible fibres can have a higher permeability than the same layer of rigid fibres due to a flow-induced deformation. Moreover, as shown by Schubauer, Spangenberg & Klebanoff (1950), the angle of the screen relative to the laminar upstream free flow has an impact on the pressure drop. Kalugin *et al.* (2021) explained also that for inclined perforated plates, the structure of the flow in the holes depends on (1) the distance of the hole on the plate from the leading edge, and (2) the angle of attack of the plate. For a low angle of attack, the effective hole area can be significantly reduced due to the difficulty of the flow to deflect from its original direction mostly parallel to the surface of the plate. All these studies underline the current difficulty to obtain a general formulation of the pressure loss for an arbitrary porous screen. Therefore, in what follows, we adopt another method based on empirical laws in order to test whether this would be sufficient to estimate the drag accurately.

Numerous experimental investigations have shown that the pressure drop can be reasonably considered proportional to the square of the velocity normal to the screen at the vicinity of it through the resistance coefficient k, especially Taylor & Davies (1944). More recently, Ito & Garry (1998) studied this problem in the 2-D case of a flow around and through a gauze for low resistance coefficient, while Eckert & Pflüger (1942) studied the resistance coefficient for the case of a gauze spanning the entire section of a channel. In these cases, the pressure drop can be written as

$$\Delta p = \tfrac{1}{2} k \rho v_{I_n}^2 (x_s, y_s, z_s). \tag{4.2}$$

The resistance coefficient k depends on the geometry of the holes, the material of the screen and the Reynolds number based on the scale of the holes (sometimes k is directly related to what is called the loss factor or friction factor). This has been mostly studied when the screen spans entirely a channel with normal incidence, and oblique incidence (Schubauer *et al.* 1950; Reynolds 1969). Note that in (3.18), $\theta(s)$ can be interpreted as a resistance coefficient, the intervention of the tangential velocity in (3.18) comes from the fact that in our case the fluid can pass around the porous structure.

To formulate the resistance coefficient dependency for porous screens, Pinker & Herbert (1967) has shown that the resistance coefficient k can reasonably be considered as a product of a function of the solidity, $G(s)$, and a function f of the local Reynolds number in a pore. In our definition of Re_d, we use the upstream velocity of the fluid far from the mesh; in order to take into account the changes in velocity close to the mesh, we define the local approach Reynolds number,

$$Re_n = Re_d \frac{v_{I_n}}{v_0}, \tag{4.3}$$

based on the scale of holes and the approach velocity that in our formulation corresponds to v_{I_n}. Among several fitted expressions for G with respect to the solidity, Pinker & Herbert (1967) found that $G(s) = -\theta(s)$, which exhibits the best agreement with their data.

For the pressure drop, depending also on the inclination of the surface, we have to consider in fact the function $f(Re_n, \beta)$, as first proposed by Schubauer *et al.* (1950). Since the geometry of our porous screen is arbitrary, β should be considered as a local characteristic of the inclination of the surface of the screen relative to the direction of the laminar free flow in the far upstream. Here $\beta = 0$ means that the surface is parallel to the

flow $\boldsymbol{v}_0$. We thus propose the following relation for the pressure jump:

$$p_{II}(x_s, y_s, z_s) - p_I(x_s, y_s, z_s) = \tfrac{1}{2}\rho v_{I_t}^2(x_s, y_s, z_s)(1 - E^2(\psi_I, \chi_I)) + \tfrac{1}{2}\rho v_{I_n}^2(x_s, y_s, z_s)\theta(s) f(Re_n, \beta). \tag{4.4}$$

The expression of f is thus expected to be found experimentally. As far as we know, there is no general physical formulation of the pressure drop through the holes at the microscopic level that can cover all types of screens, and there is no general demonstration of an analytical expression of f for an arbitrary porous screen shape. Therefore, it is expected that some modifications are required for particular porous structures taking into account, for instance, the geometry of the holes. For screens composed of fibres, with an angle of attack β with the upstream flow, and for $10^{-4} < Re_n < 10^4$, Brundrett (1993) gives the following empirical expression of f:

$$f(Re_n, \beta) = \sin^2(\beta)\left(\frac{c_1}{Re_n \sin(\beta)} + \frac{c_2}{\ln(Re_n \sin(\beta) + 1.25)} + c_3 \ln(Re_n \sin(\beta))\right). \tag{4.5}$$

Here c_1, c_2 and c_3 are real constant. In this model (4.5), the first term corresponds to the laminar contribution, the second term to the turbulent friction and the last term is valid at large Reynolds numbers (Brundrett 1993). Brundrett (1993) obtain a good fitting with his data for wire mesh screens by taking $c_1 \approx 7.125$, $c_2 \approx 0.88$, $c_3 \approx 0.055$. Bailey *et al.* (2003) found also a good fitting with their data by taking $c_1 \approx 18$, $c_2 \approx 0.75$ and $c_3 \approx 0.055$. For the following sections of the paper, we take the geometric mean of the different values $c_1 \approx 11$, $c_2 \approx 0.8$ and $c_3 \approx 0.055$. For high Re_n, the function f behaves as a logarithmic function of the Reynolds number Re_n, while for low Re_n, the variation of f is much more pronounced (inverse function of the Reynolds number Re_n). We thus expect the viscous effects to be important for the typical flow speeds and mesh sizes considered in this work, and in applications such as fog harvesting and face masks.

We thus use this empirical expression, which is in principle only valid for fibrous screens, to account for local viscous effects in our experiments. The last term in the pressure jump (3.18) is thus multiplied by $f(\beta, Re_n)$. This is carried through all the calculation. In particular, our equation to determine the source strength (3.50) is modified such that

$$-\tfrac{1}{8}\omega^4\theta(s) f(Re_n, \beta) + \omega^2 \sin^2(\beta)(8\gamma_0 + \theta(s) f(Re_n, \beta) - 2) - 4\omega \sin(\beta) - 2\sin^4(\beta)\theta(s) f(Re_n, \beta) = 0. \tag{4.6}$$

This equation has been solved using Python 3.9.5 and the method fsolve from scipy.optimize. In the following, we keep and compare both formulations (3.50) and (4.6). For high solidity, and for a certain range of the two Reynolds numbers Re and Re_d, the term $\theta(s) f(Re_n, \beta)$ should behave as the inertial term of the Darcy–Forchheimer equation for porous media. For porous screens composed of square fibre meshes, the inertial term of the Darcy–Forchheimer equation calculated with the method of Wang *et al.* (2021) has a value reasonably close to $\theta(s)$ when $s \approx 0.9$. For a very thin porous surface, as discussed by Teitel (2010), the concept of permeability for porous media involved in the equation of Darcy, and Darcy–Forshheimer, may not always hold for the pressure loss through screens depending on the regime of the flow. According to Brundrett (1993) and Bailey *et al.* (2003), the expression (4.5) seems to be valid over a larger flow regime.

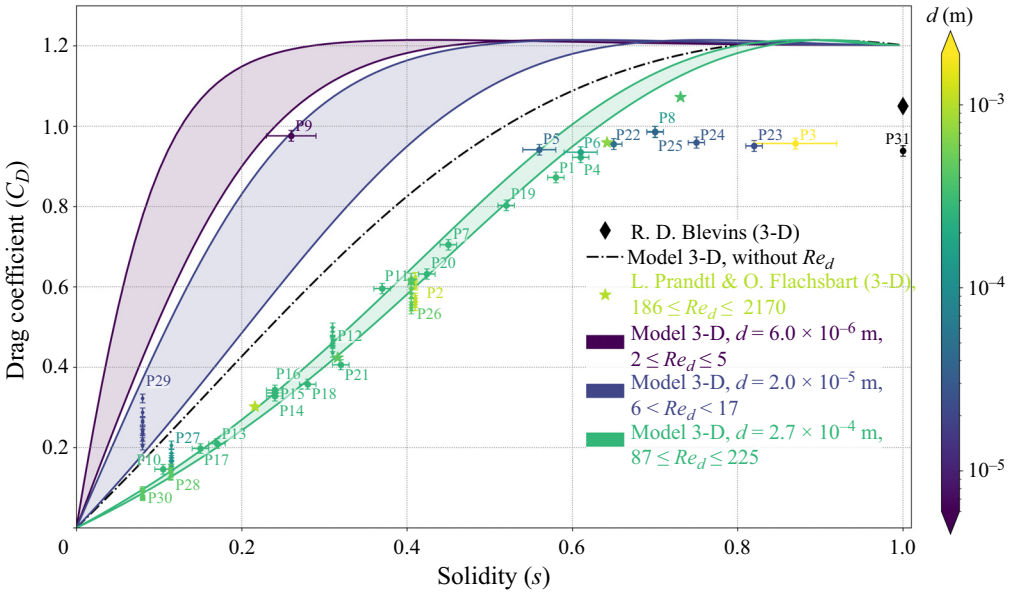

Figure 10. Drag coefficient as a function of the solidity for various square porous screens normal to the free flow with different Re_d, and comparison between the 3-D model. The full lines are obtained with the 3-D model developed in this paper, solution of (4.6). The black dash-dotted curve is the solution of (3.50), thus, without taking into account Re_d.

4.2. *Three-dimensional and viscous effects on the drag coefficient*

As seen previously, our experiments suggest a strong effect of the local Reynolds number on the drag coefficient. We now compare in figure 10 our experimental results with the prediction of the 3-D model, including local viscous effects using the function $f(Re_n, \beta)$. For all mesh Reynolds numbers Re_d, the trend of the curve remains globally the same: there is an approximately linear increase of the drag coefficient at low solidity before the curve flattens and reaches a plateau, which is well represented by the 3-D model derived using the method proposed by Steiros & Hultmark (2018), i.e. without $f(Re_n, \beta)$ (3.50). However, the slope of the initial linear part strongly depends on Re_d: it decreases with increasing mesh Reynolds number Re_d for $Re_d < 10^3$.

Using our model, (4.4) with the empirical formulation of Brundrett (1993), we obtain a good fitting with our data for solidity $s \leq 0.6$, for different Reynolds numbers. This shows the importance of both the 3-D effects and the viscous effects through the local Reynolds number Re_d. In particular, for a given solidity, the drag coefficient strongly decreases for increasing Re_d, as are plotted in figure 11.

We indeed observe a strong effect of the mesh Reynolds number, that also depends on the solidity. We observe a decrease of drag coefficient with increasing Re_d that is well captured by the empirical formulation (4.6). This effect has also been observed for perforated plates by de Bray (1957). At low Re_d, all curves tend towards the value of the drag coefficient of a flat solid plate, i.e. no fluid is passing through the screen and most of it is deviated around. We then note rapid variations for intermediate values of Re_d ($5 < Re_d < 50$ depending on the solidity), to finally converge towards a constant value at high Re_d. This reduction of drag decreases with increasing solidity. As expected, for high solidity ($s = 0.9$), there are no effects of Re_d, as the flow through the screen is weak. We obtain a similar drag coefficient using the values for the constants c_1, c_2 and c_3 from either

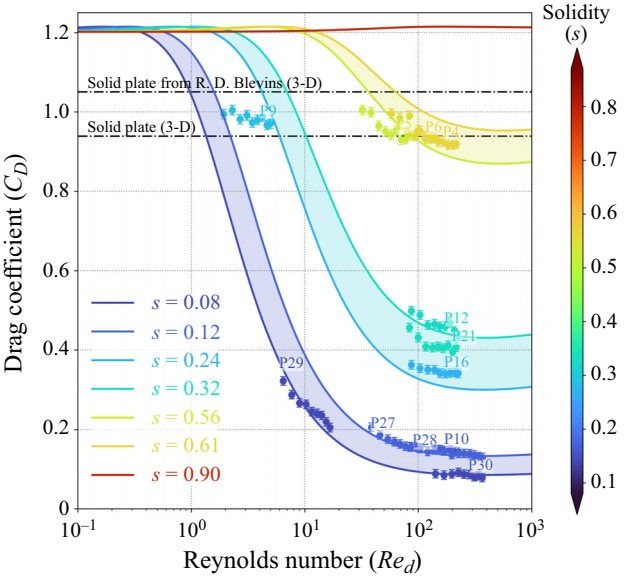

Figure 11. Drag coefficient as a function of the Reynolds number Re_d for three different narrow ranges of solidities: $s = 0.1 \pm 0.02$, $s = 0.28 \pm 0.04$, $s = 0.585 \pm 0.025$. The bullets represent the experimental measurements, and the plain lines the results of our model ((4.6) taking into account the effect of mesh Reynolds number Re_d). The data points for the drag as well as the Reynolds number values are obtained for the velocity $5.0 \leq v_0 \leq 13\,\mathrm{m\,s^{-1}}$. The dash-dotted lines represent the value of the drag coefficient for a solid plate (three dimensional) from our experiments and from Blevins (1992).

Brundrett (1993) or Bailey *et al.* (2003). Indeed, we see that for all solidity and moderate Reynolds numbers $Re_d = O(200)$ that correspond to most of the screens we tested, the difference is small ($1 \leq C_D(\text{Bailey})/C_D(\text{Brundrett}) \leq 1.05$), and the difference is even lower with increasing Reynolds number Re_d. For low Reynolds numbers $Re_d = O(5)$, the difference is however higher.

To further check the validity of our model, we made screens that have the same solidity but different hole size and number, keeping however Re_d constant (see table 1 for $s = 0.24$ (P14, P15 and P16) and $s = 0.7$ (P8 and P25)), but still with a periodic distribution. As expected from our model, we do not observe any difference in the drag coefficient within the bounds of the measurement uncertainty, demonstrating that for these regular screens, the friction coefficient depends only on s and Re_d.

4.3. *Flow visualization*

We can gain some insights into those behaviours by plotting the streamlines and velocity magnitude of the flow around and through the screen with our model (figure 12). For a screen normal to the flow, we observe that as the solidity increases, a larger part of the flow is deviated around the screen and that the flow is strongly slowed down in front of the screen, which is consistent with the measured increase of drag coefficient (figure 12*a–c*).

This analysis is taken further by plotting in figure 13 both the PIV measurements (as described in § 2) in the symmetry plane of the screen, as well as the theoretical predictions using the pressure jump equation (3.18) for the sake of simplicity (thus, not accounting for the mesh Reynolds number Re_d effect). As the solidity increases, we can observe a stronger attenuation of the velocity behind the screen, a larger deviation of the flow around the

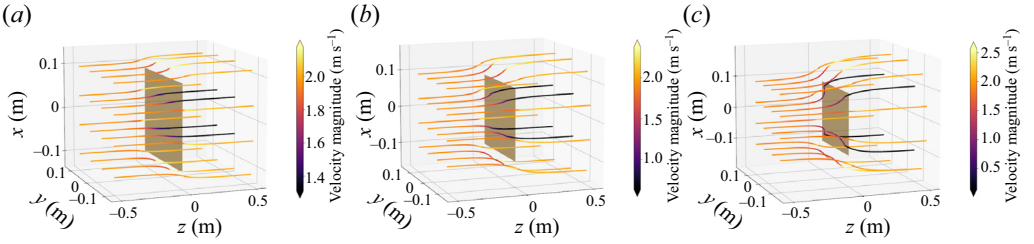

Figure 12. Streamlines and velocity magnitude obtained with the 3-D model for a square screen normal to the flow at $v_0 = 2.0\,\mathrm{m\,s^{-1}}$ for different solidities and the pressure jump defined in (3.18) (thus, without dependency on the mesh Reynolds number Re_d). Results are shown for (*a*) $s = 0.3$ and $\beta = 90°$; (*b*) $s = 0.6$ and $\beta = 90°$; (*c*) $s = 0.9$ and $\beta = 90°$.

Screen number	P1	P4	P7	P8	P9	P14	P19	P21	P22	P23	P25	P27	P28
Reynolds number Re_d	53	47	49	24	0.16–3.5 mean 0.75	49	47	47	9.1	5.0	6.7	22	80

Table 2. Reynolds number Re_d calculated with the fibre diameter d as characteristic size and with a velocity $v_0 = 2.84\,\mathrm{m\,s^{-1}}$ and a kinematic viscosity $\nu = 15.6 \times 10^{-6}\,\mathrm{m^2\,s^{-1}}$.

screen, as well as the apparition of a slower region upstream of the screen. We note that the theoretical prediction of the velocity magnitudes are in good agreement with the measured velocities even for the velocity attenuation downstream in the wake. We also observe that the attenuation of the velocity upstream is well captured by the model. However, for high solidity, the width of the wake appears larger in experiments than in the model, which might also be due to the presence of a thicker frame around the mesh in the experiments. Indeed, as observed in the streamlines in figure 4, there are vortices attached to the edges of the frame that may impact both the normal velocity and the shape of the wake.

By mass conservation and since the normal velocity is assumed constant on the surface in this study, the proportion of the incoming fluid that goes through the screen is directly given by the dimensionless normal velocity v_n/v_0. Experimentally, we measure the velocity using a constant temperature anemometer from Dantec Dynamics (MiniCTA, with probe 55P11, tungsten wire with diameter 5 µm and length 1.25 mm, precision of $0.01\,\mathrm{m\,s^{-1}}$, minimum velocity of $0.20\,\mathrm{m\,s^{-1}}$). In figure 14 we plot this ratio v_{I_n}/v_0 as a function of the solidity s for different meshes, i.e. different Re_d as presented in table 2. For a high mesh Reynolds number and low solidity, the model exhibits good agreements with the data. However, we observe a strong effect of Re_d on the normal velocity: notably, for a small mesh Reynolds number Re_d, the normal velocity drops more rapidly than predicted by the model. The model also overpredicts the normal velocity for high solidity. For screens commonly used for fog harvesting ($Re_d = O(100)$), the normal velocity in the case where Re_d is taken into account can be up to 21 % greater than the normal velocity in the case where Re_d is not taken into account (according to our theoretical results, this is true for $0.25 < s < 0.75$), and is thus not negligible. These data are coherent with the PIV measurements.

In figure 15 we plot the dimensionless tangential velocity distribution on the porous surface for different solidities s and Reynolds number Re_d. We see that the tangential velocity is much lower than v_0 for a large part of the screen. We thus expect important

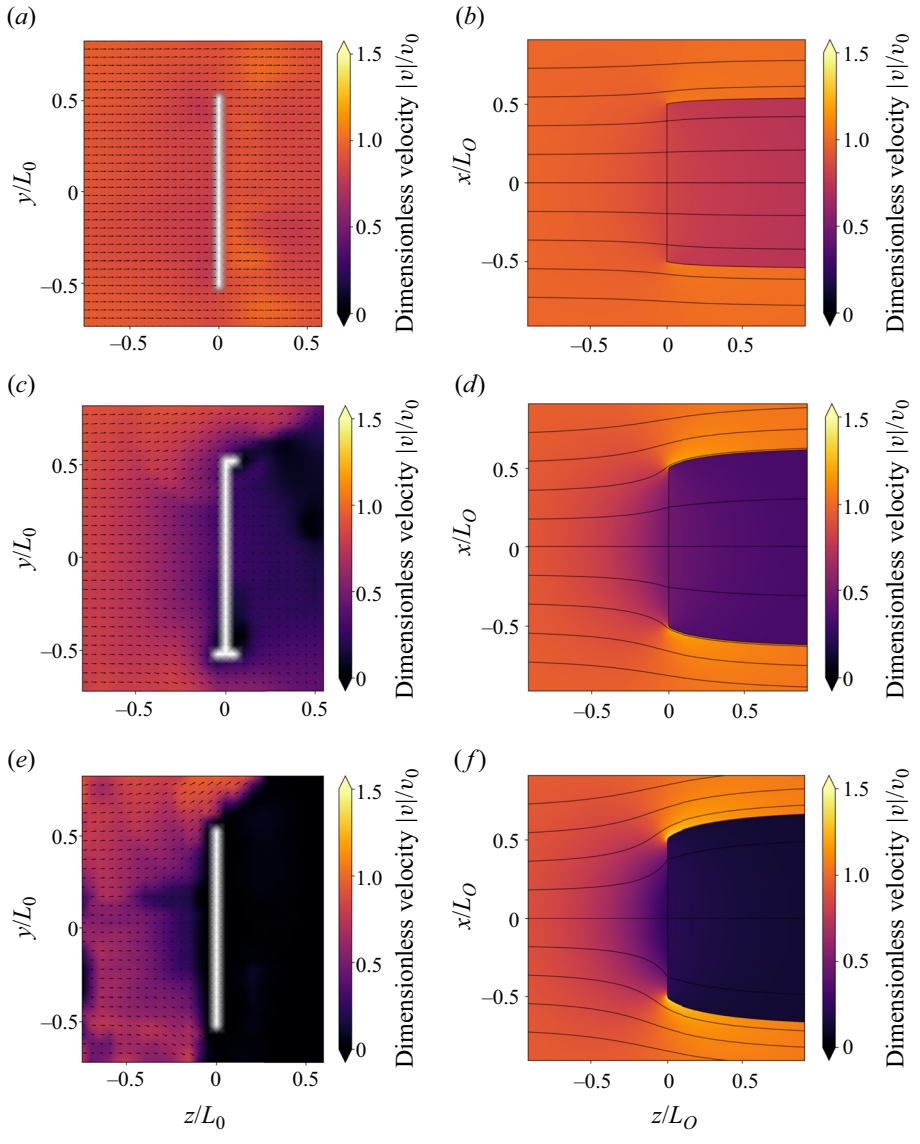

Figure 13. Comparison between the 3-D theoretical model and our experiments for the prediction of the velocity field in the (z, x) plane with $y = 0$ for three different solidities (low, moderate and high). The theoretical velocity field has been obtained using the theoretical pressure jump law (3.18) and (3.19). Uncertainties on the velocities are estimated to be around $0.1\,\mathrm{m\,s^{-1}}$. Results are shown for (*a*) P14, $s = 0.24$, experimental; (*b*) P14, $s = 0.24$, theoretical; (*c*) P6, $s = 0.61$, experimental; (*d*) P6, $s = 0.61$, theoretical; (*e*) P23, $s = 0.82$, experimental; (*f*) P23, $s = 0.82$, theoretical.

differences in the streamlines that are deviated around the screen when the solidity or Re_d varies.

In figure 16 we give a representation of the proportion of the fluid passing through the porous surface (and thus, the proportion of the fluid going around it) for different solidities and Reynolds numbers ($Re_d = 10$ and $Re_d = 100$). The contours of these sections S_a represent the separation between the fluid going through the surface and the fluid going around the surface at $z = -\infty$, i.e. the section of the streamtube or separation surface.

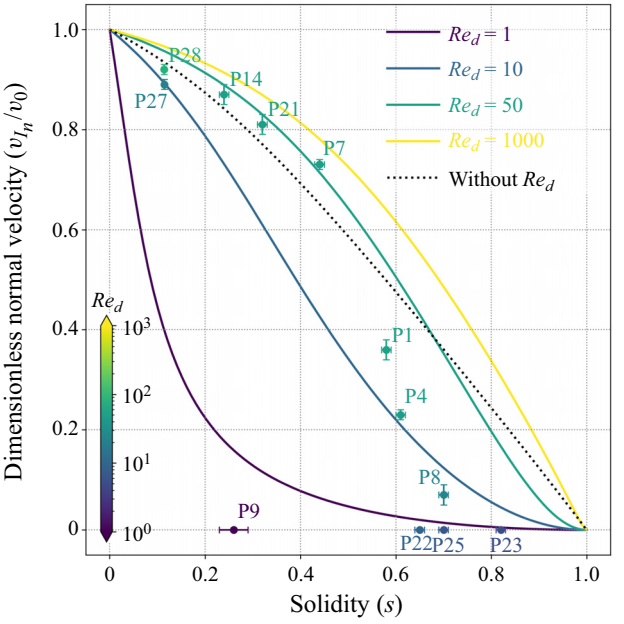

Figure 14. Dimensionless normal velocity v_{I_n}/v_0 obtained with (4.6) for the solid lines, and with (3.50) for the dotted black line. The bullets represent the experimental measurements obtained using a hot wire anemometer.

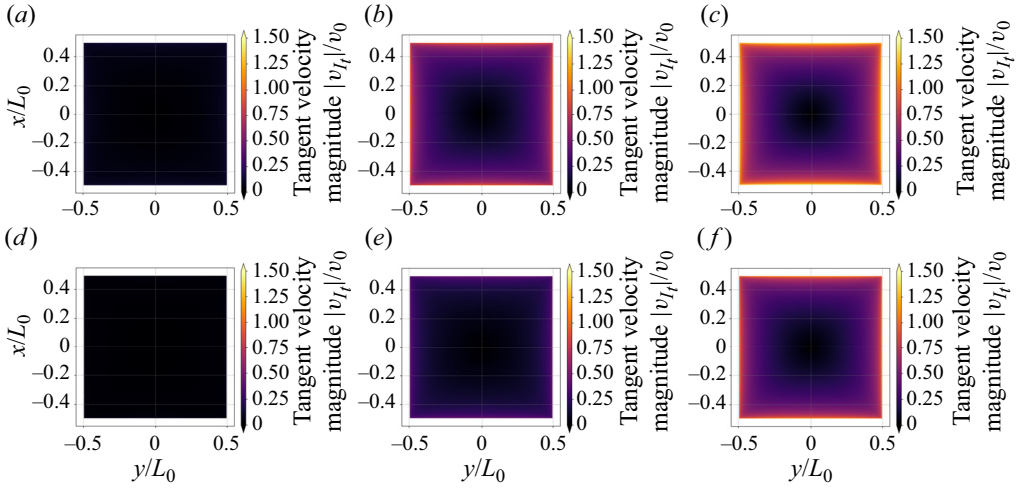

Figure 15. Dimensionless tangential velocity magnitude $|v_{I_t}|/v_0$ on the screen surface obtained with the 3-D model for a square screen normal to a flow for different solidities and Reynolds numbers ((4.6) taking into account the effect of mesh Reynolds number Re_d). Results are shown for (*a–c*) $Re_d = 10$; (*d–f*) $Re_d = 100$; (*a*) $s = 0.1$ and $Re_d = 10$; (*b*) $s = 0.5$ and $Re_d = 10$; (*c*) $s = 0.8$ and $Re_d = 10$; (*d*) $s = 0.1$ and $Re_d = 100$; (*e*) $s = 0.5$ and $Re_d = 100$; (*f*) $s = 0.8$ and $Re_d = 100$.

If we place a passive tracer inside these sections at $z = -\infty$ then the passive tracer will flow across the surface. We observe a clear effect of the 3-D nature of the flow on these separation surfaces. As measured in our experiments, the separation distance along a diagonal is much higher than along the transverse direction, and this effect is amplified as s increases and Re_d decreases. The fraction S_a/S_0 is always equal to v_n/v_0. However, in

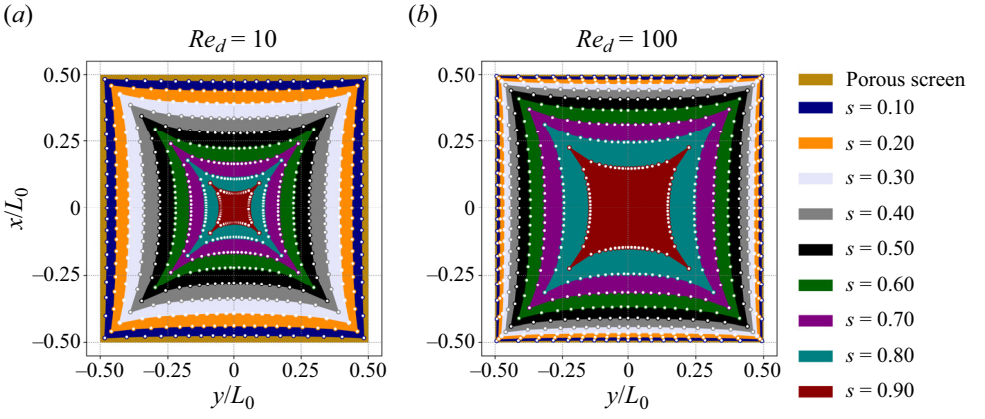

Figure 16. Upstream section S_a of the streamtube containing all the fluid passing through the surface, at $z = -\infty$, seen from the front, for $Re_d = 10$ and $Re_d = 100$.

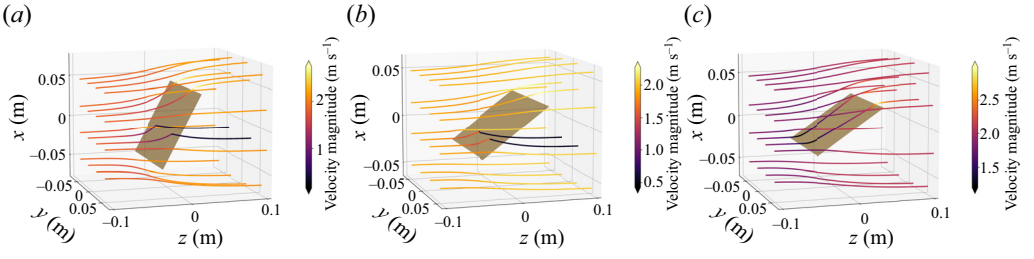

Figure 17. Streamlines and velocity magnitude obtained with the 3-D model for a square screen inclined to a flow at $v_0 = 2.0\,\mathrm{m\,s^{-1}}$ for different solidities and the pressure jump defined in (3.18) (thus, without dependency on the mesh Reynolds number Re_d). Results are shown for (*a*) $s = 0.8$ and $\beta = 60°$; (*b*) $s = 0.8$ and $\beta = 30°$; (*c*) $s = 1$ and $\beta = 30°$.

applications such as filtration or fog harvesting, where the main drop capture mechanism is inertial impact (Moncuquet *et al.* 2022), the tangential velocity and the shape of the streamlines are expected to impact the amount of droplets that leave the streamlines and are collected on the fibres.

4.4. *Drag coefficient for low angle of attack*

We then vary the orientation angle of the screen in the flow β. When the orientation angle is increased away from the normal incidence, the deviation of the streamlines is less important and the velocity is slightly higher (figure 17*a*,*b*). For the extreme case of a solid plate in figure 17(*c*), two streamlines are deviated along the plate, the flow slows down first and increases again with a peak value above the plate as the fluid particle leaves it and is re-entrained in the surrounding flow. However, if the asymptotic behaviour of the model may provide some indications about the global flow and the aerodynamic forces, it is expected to be outside of the assumptions of the model as discussed in the next section.

The experimental results are compared with our model for the two angles $\beta = 65°$ and $\beta = 43°$ on figure 18. As for panels at a normal incidence, the drag coefficient increases with increasing solidity. The drag coefficient decreases with decreasing angle of attack, i.e. as we get further away from the normal incidence. Our model is in good agreement with the experimental data at $\beta = 65°$ (figure 18*a*). However, it underestimates the drag

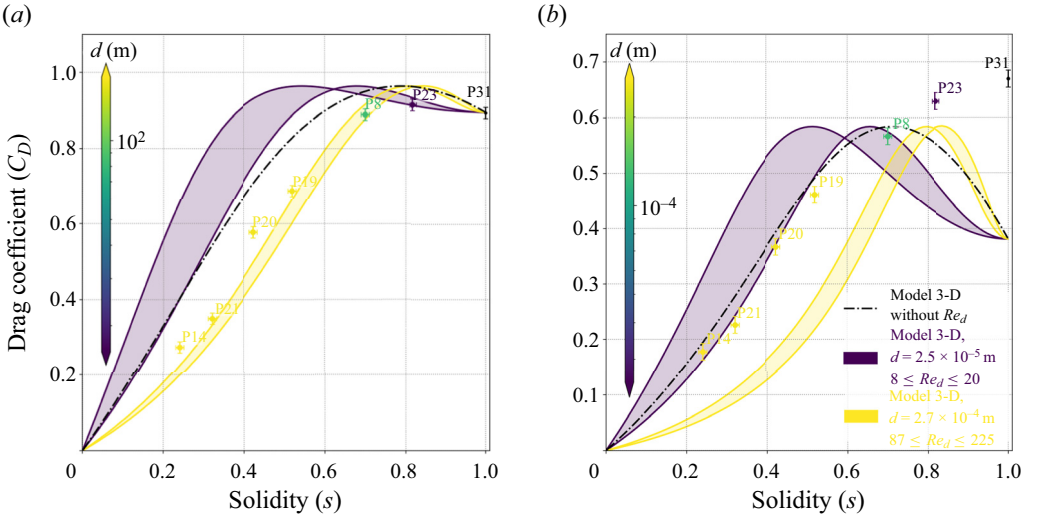

Figure 18. Comparison between the 3-D model and our experiments for the prediction of the drag coefficient at two angles of inclination for various porous square screens: (*a*) $\beta = 65^\circ$ (*b*) $\beta = 43^\circ$ using (3.50). The black dash-dotted line is the theoretical result obtained with (4.6).

at orientations further from the normal incidence ($\beta = 43^\circ$ figure 18*b*). In the case of an inclined porous screen composed of fibres, the effective solidity should increase as the angle of attack decreases. The use of this effective solidity would result in shifting our data closer to the yellow curve ($87 \leq Re_d \leq 225$) in figure 18(*b*). We finally observe that both the slope of the linear part and the final value at $s = 1$ depend on the angle and that the drag coefficient decreases with decreasing angle.

In addition, our model predicts a maximum of the drag coefficient at high solidity, as shown in figure 3 (or 10) and more pronounced in figure 18. Such a non-monotonic behaviour of the drag coefficient of permeable shells with solidity has been shown and demonstrated in the viscous regime for Stokes flow by Ledda *et al.* (2021). In our case, at high Re_L and a square screen normal to the flow, several of the porous screens have indeed (on average) a higher drag coefficient than a solid screen (e.g. for P3, P5, P8, P9, P22, P23, P24 and P25). However, due to the uncertainty and the interference drag with the frame used for the support of the screens (see Appendix C), the difference is not significant enough to draw a clear conclusion. We do not observe such a maximum in our measurements for inclined plates at an angle 43°. However, for an angle of 65°, the drag coefficient of the screen *P*23 is on average higher than the solid screen. It is also possible that in our experiments we were outside the flow regime for such a non-monotonic behaviour in the drag coefficient.

5. Model extensions

5.1. *Vena contracta*

In our model, as done also by Steiros & Hultmark (2018), we neglected the possible contraction of the flow within the holes. Considering the vena contracta within the pores, as shown in figure 19, the characteristic velocity immediately upstream given by (3.14), i.e. the mean velocity after contraction of the flow within the holes v_{h1}, can be

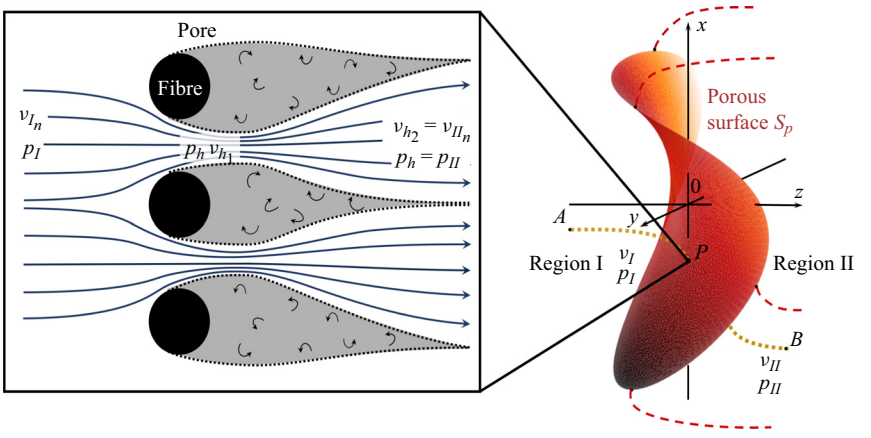

Figure 19. Diagram of the flow at the scale of the pores in case of parallel fibres (left), and corresponding imaginary surface as used in the model (right).

expressed as

$$v_{h1} = \frac{v_{In}(x_s, y_s, z_s)}{C(1-s)}, \tag{5.1}$$

where C is the contraction coefficient. This implies that the coefficient $\theta(s)$ given in (3.19) is

$$\theta(s) = 1 - \frac{1}{C^2(1-s)^2}. \tag{5.2}$$

As far as we know, there are no measurements of vena contracta for screens constituted of fibres and especially in the 3-D case of free flow. Simmons & Cowdrey (1945) performed measurements of the velocity profile behind a porous screen made of a square mesh of woven material spanning a section of a channel and suggest an estimate of the vena contracta assuming a uniform velocity $v_{h1} = v_0$ in the holes. In these experiments the screens are made of circular rods with diameters ranging from 0.112 to 0.373 mm arranged in a square mesh. The velocity used was from 2.44 to 10.36 m s^{-1}. The local Reynolds number Re_d thus varies from 18 to 248, which is the same order of most of the porous screens used in our experiments. For a solidity $s \approx 0.5$, the coefficient C should be between 0.9 and 1.0. Note that with the formulation (5.2), if $C \neq 1$, the limit $s = 0$ leads to a non-zero pressure difference, suggesting that C may depend on the solidity s at least for low solidities. We note that if the contraction of the flow is not neglected in $\theta(s)$, i.e. $C \neq 1$, there is an increase of the drag coefficient compared with the curve plotted in figure 9(*a*). We would thus still overestimate the drag compared with our data in figure 3.

5.2. *Asymptotic behaviour at large solidities*

Although the model is built for porous surfaces, it is interesting to explore its asymptotic behaviour when the solidity tends to 1. In this limit, one can question whether a porous description of the surface is still valid.

When the screen tends to a solidity equal to one, we can obtain an expression of the drag coefficient. Taking (4.6), dividing by $\theta(s)$, which tends to $+\infty$ when $s \to 1$, we have

$$(\omega^2 - 4\sin^2(\beta))^2 = 0. \tag{5.3}$$

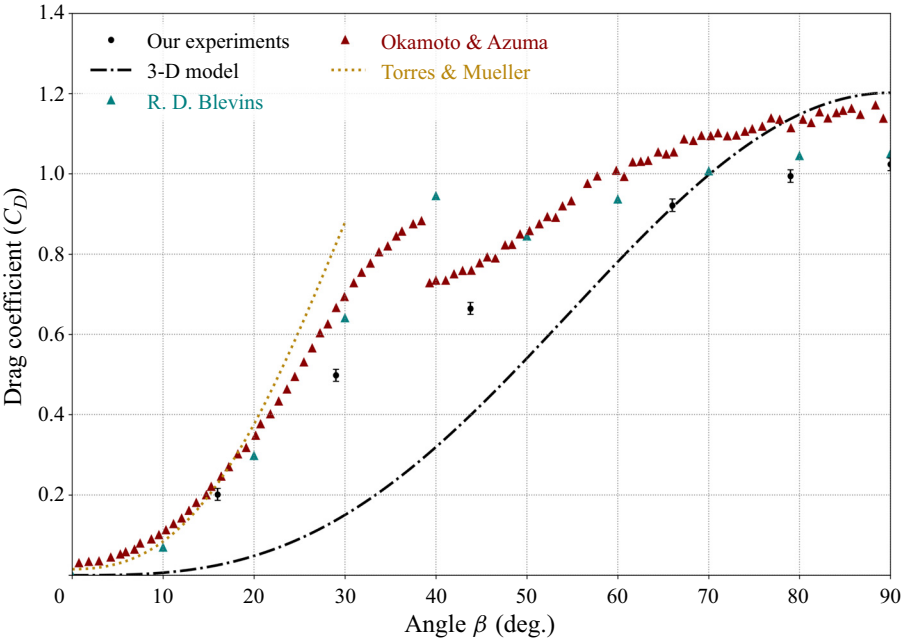

Figure 20. Comparison between the drag coefficient prediction of the 3-D model and the experimental measurement for a square plate in a free flow for different angles of inclination. Data are added from Blevins (1992), Okamoto & Azuma (2011) and Torres & Mueller (2004).

Therefore (excluding the case when ω is negative, which would not correspond to the type of flow we study in this paper), we obtain

$$\omega = 2\sin(\beta), \tag{5.4}$$

which gives $v_{In} = 0$ as expected. Introducing this value into the expression of the drag coefficient gives

$$C_D = 2\sin^3(\beta)(1 - 4\gamma_0). \tag{5.5}$$

Note that the solid drag coefficient does not depend on the assumption of the pressure loss across the screen through the expression of $\theta(s)f(Re_n, \beta)$ (in (4.4)) as expected.

We measured the drag coefficient as a function of the angle of attack for a square plate at solidity 1. We plotted the result in figure 20, and as we can see, there is a gap between the prediction (5.5) and the experimental value of the drag coefficient especially at a low angle of attack.

Several explanations for this gap can be listed. First, for the solid plate, assuming a no-slip boundary condition, the tangential component of the velocity on the surface is equal to zero and increases gradually in the boundary layer. Here, this component of the velocity is not equal to zero but takes a value that corresponds to the conservation of the pressure head along the streamlines in region I. Moreover, it is clearly possible that the pressure difference p_I–p_{II} is not always well determined through the assumptions of the model, especially for low angle of attacks (or particular shapes) where detachment of the boundary layer and the formation of separation bubbles can occur that strongly affects the pressure distribution around the surface (Crompton & Barrett 2000).

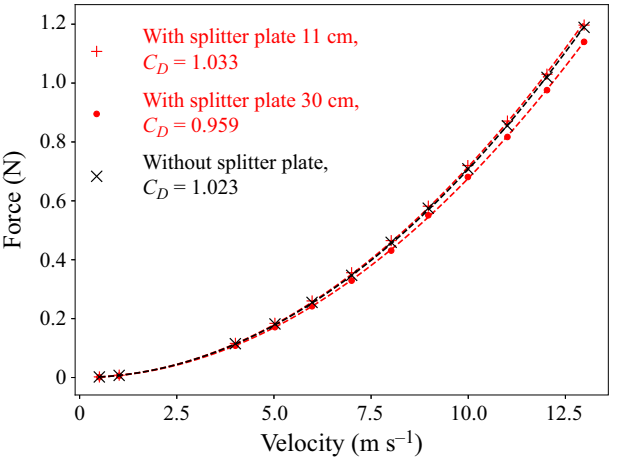

Figure 21. Comparison of the drag force F_D with and without a splitter plate for a solid plate (without frame support) of dimensions $11.0 \times 11.0\,\mathrm{cm}^2$ and thickness 3 mm. The fitting curves are obtained using a quadratic law.

5.3. *Vortex shedding*

Our model is only valid for a steady wake, i.e. without vortex shedding. This could be taken into account, but is beyond the scope of the current study. However, we believe vortex shedding has little influence on our experimental results. For instance, it has been shown that vortex shedding was suppressed for the flow past a porous cylinder (Ledda *et al.* 2018). In fact, in our flow field measurements, we do not see any vortex shedding close to the plate. To evaluate the influence of the vortex shedding on our measurements, we used two splitter plates of different length located in the wake as done by Steiros & Hultmark (2018). We note that this method was proposed for a 2-D flow, and might not apply directly to our 3-D configuration. In fact, we are not aware of experiments to suppress vortex shedding in three dimensions but we believe that splitter plates can still give pertinent information on vortex shedding. Following Apelt & West (1974), for Reynolds numbers in the range $10^4 < Re < 5 \times 10^4$, which corresponds to our case, the use of a splitter plate three times longer than the plate already suppresses the vortex shedding. In our experiments the splitter plate has the same height as the solid plate on which drag is measured but with length 11 and 30 cm and thickness of 3 mm. Figure 21 shows the measured drag force for a solid plate (solidity equal to 1, square of $11.0 \times 11.0\,\mathrm{cm}^2$, 3 mm thickness) with and without a splitter plate. We see a reduction of the drag coefficient of 0.07 with a splitter plate three times longer than the plate. This difference is expected to be less and less significant with decreasing solidity.

While these results are not sufficient to rule out completely the effect of vortex shedding, we note that vortex shedding increases the drag significantly and reduces the base pressure, as seen in drag measurements in two dimensions by Steiros & Hultmark (2018); these effects cannot explain the difference between the theory and the experimental data since suppressing vortex shedding could lead to a lower value of the drag coefficient compared with our measurements, thus, the difference between the theoretical model and the data would be more important.

6. Conclusion

We have studied both experimentally and theoretically the flow around and through porous screens. In particular, we have derived a model with a universal core based on clear physical assumptions that allows us to probe 3-D and shape effects. The main issue lies in the modelling of the pressure jump law across the screen. At low Reynolds numbers, Zampogna & Gallaire (2020) derived an analytical expression using homogenization tools. However, it is still an issue at moderate or high Reynolds numbers where no explicit relation has been derived directly from Navier–Stokes equations (Wang *et al.* 2021). We propose here to use an empirical relation obtained for fibrous screens in the literature. The semi-empirical model accurately predicts our experiments, with the only fitting parameters in the pressure jump; we note that these parameters are taken identical to those obtained in previous studies for other screens, suggesting that they are universal for any wire screens (or textiles) that are widely used in applications. For other types of screens, including perforated plates, once the pressure jump law across is known, it can be directly implemented in the model.

In addition, the empirical function includes both laminar and turbulent viscous friction, and is thus applicable to a wide range of local Reynolds numbers. The interest of the semi-empirical model lies in the fact that it uses only three types of information that are readily available: the solidity, the macroscopic geometry of the screen and the Reynolds number based on the fibre diameter. Both viscous effects (i.e. the local Reynolds number Re_d) and 3-D effects have a significant impact on the flow and aerodynamic forces. We performed experiments on more than 30 porous screens composed of fibres to measure the drag force and the flow deviation around the screen. We show both theoretically and experimentally that for screens of identical solidity, the lower the local Reynolds number based on the fibre diameter is, the higher the drag coefficient is, and the stronger the deviations are. The drag coefficient for square porous screens, either normal or with a high angle of attack, show a good agreement with the model except at very high solidity for which however the prediction is improved compared with previous models. Furthermore, the model can predict the proportion of the flow deviated around the screen, as well as the detailed separation surface and the tangential velocity, which are important quantities in many applications such as filtration or fog harvesting.

Our model might also be useful for a non-homogeneous porous screen. Indeed, for high solidity perforated square plates, de Bray (1957) found that the drag coefficient depends on the distribution of the perforations, i.e. is slightly higher with outer holes than inner holes. It is worth emphasizing that it should be possible in our model to implement such a surface with non-homogeneous solidity and, therefore, try to reproduce such a difference in the drag coefficient. However, this consideration goes beyond the scope of this paper and will be explored in a further study.

We note that this model may find an application to the wind tunnel blockage correction (Steiros *et al.* 2022) and turbines modelling (Ayati *et al.* 2019). According to Steiros *et al.* (2022), the use of a porous plate potential model as the one we use in the present paper improves the blockage correction accuracy for moderate and high solidity compared with other models. However, these models are in two dimensions (Ayati *et al.* 2019; Steiros *et al.* 2022), while the turbine can have a circular 3-D structure. Our theoretical and experimental results show that the use of a 3-D model may improve the accuracy at moderate and high solidity for the drag compared with the 2-D models (see figures 9(*a*) and 3). Moreover, our experimental results show that the normal velocity v_{I_n} on the screen may be significantly overestimated at high solidity by both 2-D and 3-D models. We stress

again that our model assumes a steady wake, and thus, is not applicable in the presence of vortex shedding that occurs at high solidity for a certain range of Reynolds numbers.

Further study should focus on more complex shapes with curvature; a straightforward formulation would be to use several small rectangular plates like the well-known panel method (adapting therefore the velocity potential ϕ). Furthermore, they should focus on the pressure and velocity distribution around the porous screen, as there are very few, if any, data for free 3-D flow. Indeed, we only found data for the drag in 3-D free flow in Prandtl & Flachsbart (1932) and more recently Letchford (2001).

Acknowledgements. We are grateful to the reviewers for their careful reading of the paper. Their detailed comments have led to an improvement of the present study.

Declaration of interests. The authors report no conflict of interest.

Author ORCIDs.
Olivier C. Marchand https://orcid.org/0000-0002-3288-087X;
Sophie Ramananarivo https://orcid.org/0000-0003-1049-4131;
Camille Duprat https://orcid.org/0000-0002-3438-4925;
Christophe Josserand https://orcid.org/0000-0003-1429-4209.

Appendix A

This appendix contains the details of the calculation of the velocities for a rectangular screen inclined with an angle β (with respect to the z axis) in a laminar flow.

Using the previous notations in § 2, the velocity potential in region I is

$$\begin{aligned}\phi_I(x, y, z) &= v_0 z + c + \phi(x, y, z)\\ &= v_0 z + c - \frac{1}{4\pi}\iint_{\mathcal{S}_p} \frac{\Omega(u, v)\,\mathrm{d}u\,\mathrm{d}v}{\sqrt{(x-v)^2 + (y - u\sin(\beta))^2 + (z - u\cos(\beta))^2}}.\end{aligned} \tag{A1}$$

A.1. *Normal component of the velocity*

From the velocity potential we deduce the velocity in region I:

$$\boldsymbol{v_I}(x, y, z) = \left(v_0 + \frac{\partial\phi}{\partial z}(x, y, z)\right)\boldsymbol{e_z} + \frac{\partial\phi}{\partial y}(x, y, z)\boldsymbol{e_y} + \frac{\partial\phi}{\partial x}(x, y, z)\boldsymbol{e_x}. \tag{A2}$$

The vector normal to the surface with an angle β is

$$\boldsymbol{e_n} = -\cos(\beta)\boldsymbol{e_y} + \sin(\beta)\boldsymbol{e_z}. \tag{A3}$$

Therefore, the component of the velocity normal to the surface is

$$\boldsymbol{v_{In}}(x, y, z) = \left(\sin(\beta)\left(v_0 + \frac{\partial\phi}{\partial z}(x, y, z)\right) - \cos(\beta)\frac{\partial\phi}{\partial y}(x, y, z)\right)\boldsymbol{e_n}, \tag{A4}$$

with

$$\frac{\partial\phi}{\partial z}(x, y, z) = \frac{1}{4\pi}\iint_{\mathcal{S}_p} \frac{(z - u\cos(\beta))\Omega(u, v)}{((x-v)^2 + (y - u\sin(\beta))^2 + (z - u\cos(\beta))^2)^{3/2}}\mathrm{d}u\,\mathrm{d}v, \tag{A5}$$

$$\frac{\partial\phi}{\partial y}(x, y, z) = \frac{1}{4\pi}\iint_{\mathcal{S}_p} \frac{(y - u\sin(\beta))\Omega(u, v)}{((x-v)^2 + (y - u\sin(\beta))^2 + (z - u\cos(\beta))^2)^{3/2}}\mathrm{d}u\,\mathrm{d}v. \tag{A6}$$

The normal velocity magnitude is therefore

$$v_{In}(x, y, z) = \sin(\beta) v_0 + \frac{1}{4\pi} I(x, y, z), \tag{A7}$$

with

$$I(x, y, z) = \iint_{\mathcal{S}_p} \frac{(\sin(\beta) z - \cos(\beta) y)\Omega(u, v)}{((x - v)^2 + (y - u\sin(\beta))^2 + (z - u\cos(\beta))^2)^{3/2}} \mathrm{d}u\,\mathrm{d}v. \tag{A8}$$

When this component is evaluated on the surface, the integral becomes singular at the position of this evaluation. We have to calculate the value of this singularity. To simplify the calculation, we introduce two parameters:

$$\left.\begin{aligned} h &= y\sin(\beta) + z\cos(\beta), \\ t &= y\cos(\beta) - z\sin(\beta). \end{aligned}\right\} \tag{A9}$$

Thus, we have inversely

$$\left.\begin{aligned} y &= h\sin(\beta) + t\cos(\beta), \\ z &= h\cos(\beta) - t\sin(\beta). \end{aligned}\right\} \tag{A10}$$

Denoting $\tilde{I}$ the integral I with the new parameters and without the source strength Ω assumed to be continuous, we obtain

$$\begin{aligned} \tilde{I}(x, h, t) &= -\int_{v_a}^{v_b} \int_{u_a}^{u_b} \frac{t}{((x - v)^2 + t^2 + (h - u)^2)^{3/2}} \mathrm{d}u\,\mathrm{d}v \\ &= F_{u_a, v_a}(x, h, t) - F_{u_b, v_a}(x, h, t) - F_{u_a, v_b}(x, h, t) + F_{u_b, v_b}(x, h, t), \end{aligned} \tag{A11}$$

with

$$F_{u_a, v_a}(x, h, t) = \arctan\left(\frac{(h - u_a)(v_a - x)}{t\sqrt{(x - v_a)^2 + t^2 + (h - u_a)^2}}\right). \tag{A12}$$

We can now introduce

$$\left.\begin{aligned} y &= w\sin(\beta), \\ z &= (w + \epsilon)\cos(\beta). \end{aligned}\right\} \tag{A13}$$

The parameters become

$$\left.\begin{aligned} h &= w, \\ t &= -\epsilon\cos(\beta)\sin(\beta). \end{aligned}\right\} \tag{A14}$$

At the surface $\epsilon \to 0^{\pm}$ ($\pm$ depending on the direction from which we approach the surface, upstream or downstream), denoting $\tilde{\tilde{I}}$ the integral I with the new parameters w,

we have

$$v_{In}(x, w) = v_n^-, \tag{A15}$$

$$v_{IIn}(x, w) = Ev_n^+, \tag{A16}$$

with

$$v_n^\pm = \sin(\beta)v_0 + \frac{1}{4\pi}\lim_{\epsilon\to 0^\pm}\tilde{\tilde{I}}(x, w). \tag{A17}$$

Whatever the constant integral bounds, we have the following limit:

$$\lim_{\epsilon\to 0^\pm}\tilde{\tilde{I}}(x, w) = \pm 2\pi\Omega(x, w). \tag{A18}$$

Therefore, the normal component of the velocity at the position (x, w) on the porous surface is

$$v_{In}(x, w) = \sin(\beta)v_0 - \tfrac{1}{2}\Omega(x, w) \tag{A19}$$

and

$$v_{IIn}(x, w) = E\left(\sin(\beta)v_0 + \tfrac{1}{2}\Omega(x, w)\right). \tag{A20}$$

A.2. *Tangential component of the velocity*

We define the tangential vector on the porous surface as

$$\boldsymbol{t} = \boldsymbol{t_1} + \boldsymbol{t_2}, \tag{A21}$$

with

$$\boldsymbol{t_1} = \boldsymbol{e_x}, \tag{A22}$$

$$\boldsymbol{t_2} = \sin(\beta)\boldsymbol{e_y} + \cos(\beta)\boldsymbol{e_z}. \tag{A23}$$

Thus, the magnitude of the tangential component of the velocity in region I is

$$\begin{aligned} v_{It}(x, y, z) &= \|(\boldsymbol{v_I}\cdot\boldsymbol{t_1})\boldsymbol{t_1} + (\boldsymbol{v_I}\cdot\boldsymbol{t_2})\boldsymbol{t_2}\| \\ &= \left(\left(\frac{\partial\phi}{\partial x}\right)^2 + \left(\sin(\beta)\frac{\partial\phi}{\partial y} + \cos(\beta)\left(v_0 + \frac{\partial\phi}{\partial z}\right)\right)^2\right)^{1/2}. \end{aligned} \tag{A24}$$

If we consider a constant source strength Ω then we can write the tangential velocity at the point (x, w) on the surface with w defined in (A13) as

$$v_{It}(x, w) = (\Omega^2\mathcal{I}_x^2(x, w) + (\Omega(\sin(\beta)\mathcal{I}_y(x, w) + \cos(\beta)\mathcal{I}_z(x, w)) + \cos(\beta)v_0)^2)^{1/2}. \tag{A25}$$

For simplicity, we use the root mean square of the magnitude of the tangential component of the velocity on the surface. We have

$$\begin{aligned} v_{It} &= \frac{1}{\sqrt{S_p}}\left(\iint_{S_p} v_{I_t}^2(x, w)\,\mathrm{d}x\,\mathrm{d}w\right)^{1/2} \\ &= (\Omega^2\gamma(\beta) + \Omega\alpha(\beta)v_0 + v_0^2\cos^2(\beta))^{1/2}, \end{aligned} \tag{A26}$$

with

$$\gamma(\beta) = \frac{1}{S_p}\iint_{\mathcal{S}_p} \mathcal{I}_x^2(x,w) + (\sin(\beta)\mathcal{I}_y(x,w) + \cos(\beta)\mathcal{I}_z(x,w))^2\,\mathrm{d}x\,\mathrm{d}w, \tag{A27}$$

and

$$\alpha(\beta) = \frac{1}{S_p}\iint_{\mathcal{S}_p} 2\cos(\beta)(\sin(\beta)\mathcal{I}_y(x,w) + \cos(\beta)\mathcal{I}_z(x,w))\,\mathrm{d}x\,\mathrm{d}w, \tag{A28}$$

with the following integrals:

$$\mathcal{I}_x(x,w) = \frac{1}{4\pi}\iint_{\mathcal{S}_p} \frac{x-v}{((x-v)^2+(w-u)^2)^{3/2}}\mathrm{d}u\,\mathrm{d}v, \tag{A29}$$

$$\mathcal{I}_y(x,w) = \frac{1}{4\pi}\iint_{\mathcal{S}_p} \frac{(w-u)\sin(\beta)}{((x-v)^2+(w-u)^2)^{3/2}}\mathrm{d}u\,\mathrm{d}v, \tag{A30}$$

$$\mathcal{I}_z(x,w) = \frac{1}{4\pi}\iint_{\mathcal{S}_p} \frac{(w-u)\cos(\beta)}{((x-v)^2+(w-u)^2)^{3/2}}\mathrm{d}u\,\mathrm{d}v. \tag{A31}$$

There is no particular difficulty to compute the integrals, if we define a function $F_{a,b} : (x,w) \mapsto F_{a,b}(x,w)$ as well as $G_{a,b} : (x,w) \mapsto G_{a,b}(x,w)$ where $|a| \geq |x|$, $|b| \geq |w|$,

$$F_{a,b}(x,w) = \frac{1}{4\pi}\ln\left(\sqrt{(x-a)^2+(w-b)^2}+w-b\right) \tag{A32}$$

and

$$G_{a,b}(x,w) = \frac{1}{4\pi}\ln\left(\sqrt{(x-a)^2+(w-b)^2}+x-a\right), \tag{A33}$$

then if we integrate over the rectangular domain $[v_a, v_b] \times [u_a, u_b]$, we have

$$\mathcal{I}_x(x,w) = F_{v_a,u_a}(x,w) - F_{v_a,u_b}(x,w) - F_{v_b,u_a}(x,w) + F_{v_b,u_b}(x,w), \tag{A34}$$

$$\begin{aligned}\mathcal{I}_y(x,w) = \sin(\beta)(&G_{v_a,u_a}(x,w) - G_{v_a,u_b}(x,w)\\ &- G_{v_b,u_a}(x,w) + G_{v_b,u_b}(x,w)),\end{aligned} \tag{A35}$$

$$\begin{aligned}\mathcal{I}_z(x,w) = \cos(\beta)(&G_{v_a,u_a}(x,w) - G_{v_a,u_b}(x,w)\\ &- G_{v_b,u_a}(x,w) + G_{v_b,u_b}(x,w)),\end{aligned} \tag{A36}$$

and those expressions are integrable again over the rectangular domain $[v_a, v_b] \times [u_a, u_b]$.

For a screen normal to the free flow $\boldsymbol{v_0}$, $\beta = \pi/2$; thus, the mean tangential velocity is reduced to

$$v_{It} = \Omega\sqrt{\gamma\left(\frac{\pi}{2}\right)}. \tag{A37}$$

A.3. *Value of the shape parameters for a rectangular screen with different aspect ratio*

Starting from (A27) and (A28) we can rewrite the expression of $\gamma(\beta)$ and $\alpha(\beta)$ in order to separate the shape terms and the inclination terms, we see for this particular case of a

Aspect ratio	l_1	l_2	γ_0
1	0.1	0.1	0.0998
2	0.1	0.2	0.0977
4	0.1	0.4	0.0934
8	0.1	0.8	0.0894
10	0.1	1.0	0.0884
20	0.1	2.0	0.0861

Table 3. Shape parameter for rectangular plate with different aspect ratios. Here l_1 and l_2 are the lengths of the sides of the rectangular plate. The aspect ratio is l_2/l_1.

rectangular plate that these expressions can be simplified as

$$\gamma(\beta) = \gamma_0 \tag{A38}$$

and

$$\alpha(\beta) = 2\alpha_0 \cos(\beta), \tag{A39}$$

with

$$\begin{aligned}\mathcal{J}(x, w) &= \frac{1}{4\pi} \iint_{\mathcal{S}_p} \frac{w-u}{((x-v)^2 + (w-u)^2)^{3/2}} \mathrm{d}u\, \mathrm{d}v \\ &= G_{v_a,u_a}(x, w) - G_{v_a,u_b}(x, w) - G_{v_b,u_a}(x, w) + G_{v_b,u_b}(x, w),\end{aligned} \tag{A40}$$

$$\left.\begin{aligned}\gamma_0 &= \frac{1}{S_p} \iint_{\mathcal{S}_p} \mathcal{I}_x^2(x, w) + \mathcal{J}^2(x, w)\, \mathrm{d}x\, \mathrm{d}w, \\ \alpha_0 &= \frac{1}{S_p} \iint_{\mathcal{S}_p} \mathcal{J}(x, w)\, \mathrm{d}x\, \mathrm{d}w.\end{aligned}\right\} \tag{A41}$$

For symmetry reasons, $\alpha_0 = 0$. Thus, the mean tangential component of the velocity at the surface for a rectangular plate inclined in the flow is actually

$$v_{It} = (\Omega^2 \gamma_0 + v_0^2 \cos^2(\beta))^{1/2}. \tag{A42}$$

We computed the values of the parameter γ_0 in table 3 for different aspect ratios ($v_b = -v_a = l_1/2$ and $u_b = -u_a = l_2/2$). We used Python 3.9.5 with the method nquad from scipy.integrate.

Appendix B

This appendix contains the details of the calculation of the source strength Ω for the case of a rectangular screen inclined to the laminar free flow with an angle β with respect to the z axis. We start from the following equations.

The pressure difference is expressed as

$$p_{II} - p_I = \tfrac{1}{2}\rho(v_{I_t}^2(1-E^2) + v_{I_n}^2\theta(s)f(Re_n,\beta)), \tag{B1}$$

$$p_{III} - p_0 = \tfrac{1}{2}\rho((1-E^2)v_0^2 + v_{I_n}^2\theta(s)f(Re_n,\beta)). \tag{B2}$$

The drag forces are expressed as

$$F_D = \rho v_0(1-E)v_n S_p + \frac{1}{v_0}(p_0{-}p_{III})\frac{v_n}{E}S_p, \tag{B3}$$

$$F_D = (p_I{-}p_{II})\sin(\beta)S_p + \rho v_n v_0 \cos^2(\beta)(1-E)S_p. \tag{B4}$$

In these expressions the normal and tangential components of the velocity at the surface of the screen are

$$v_{In} = \sin(\beta)v_0 - \tfrac{1}{2}\Omega, \tag{B5}$$

$$v_{It} = (\Omega^2\gamma_0 + v_0^2\cos^2(\beta))^{1/2}. \tag{B6}$$

Then, by denoting $\omega = \Omega/v_0$ we have, for the velocities,

$$\frac{v_{In}}{v_0} = \sin(\beta) - \frac{1}{2}\omega, \tag{B7}$$

$$\frac{v_{It}}{v_0} = (\omega^2\gamma_0 + \cos^2(\beta))^{1/2}. \tag{B8}$$

The attenuation coefficient E is

$$E = \frac{\sin(\beta) - \dfrac{1}{2}\omega}{\sin(\beta) + \dfrac{1}{2}\omega}. \tag{B9}$$

For the pressure differences, we obtain

$$\frac{p_{II} - p_I}{\dfrac{1}{2}\rho v_0^2} = (\omega^2\gamma_0 + \cos^2(\beta))\frac{2\omega\sin(\beta)}{\left(\sin(\beta) + \dfrac{1}{2}\omega\right)^2} + \left(\sin(\beta) - \frac{1}{2}\omega\right)^2\theta(s)f(Re_n,\beta), \tag{B10}$$

$$\frac{p_{III} - p_0}{\dfrac{1}{2}\rho v_0^2} = \frac{2\omega\sin(\beta)}{\left(\sin(\beta) + \dfrac{1}{2}\omega\right)^2} + \left(\sin(\beta) - \frac{1}{2}\omega\right)^2\theta(s)f(Re,\beta). \tag{B11}$$

The first expression of the drag force is

$$\frac{F_D}{\dfrac{1}{2}\rho v_0^2 S_p} = \frac{2\omega\left(\sin(\beta) - \dfrac{1}{2}\omega\right)}{\sin(\beta) + \dfrac{1}{2}\omega} + \left(\sin(\beta) + \frac{1}{2}\omega\right)\frac{p_0{-}p_{III}}{\dfrac{1}{2}\rho v_0^2}. \tag{B12}$$

The second expression of the drag force is

$$\frac{F_D}{\frac{1}{2}\rho v_0^2 S_p} = \frac{p_I - p_{II}}{\frac{1}{2}\rho v_0^2}\sin(\beta) + \cos^2(\beta)\frac{2\omega\left(\sin(\beta) - \frac{1}{2}\omega\right)}{\sin(\beta) + \frac{1}{2}\omega}. \tag{B13}$$

The two expressions of the drag coefficient are

$$C_D = \frac{-\omega^2}{\sin(\beta) + \frac{1}{2}\omega} - \left(\sin(\beta) + \frac{1}{2}\omega\right)\left(\sin(\beta) - \frac{1}{2}\omega\right)^2 \theta(s) f(Re_n, \beta), \tag{B14}$$

$$\begin{aligned} C_D = {} & \cos^2(\beta)\frac{2x\left(\sin(\beta) - \frac{1}{2}\omega\right)}{\sin(\beta) + \frac{1}{2}\omega} - \sin(\beta)\left(\sin(\beta) - \frac{1}{2}\omega\right)^2 \theta(s) f(Re_n, \beta) \\ & - (\omega^2\gamma_0 + \cos^2(\beta))\frac{2\omega\sin^2(\beta)}{\left(\sin(\beta) + \frac{1}{2}\omega\right)^2}. \end{aligned} \tag{B15}$$

By combining the expression (B14) and (B15), we obtain the equation

$$\begin{aligned} & -\tfrac{1}{8}\omega^4\theta(s) f(Re_n, \beta) + \omega^2\sin^2(\beta)(8\gamma_0 + \theta(s) f(Re_n, \beta) - 2) \\ & - 4\omega\sin(\beta) - 2\sin^4(\beta)\theta(s) f(Re_n, \beta) = 0. \end{aligned} \tag{B16}$$

Note that, for a rectangular screen normal to the free flow, this equation is reduced to

$$-\tfrac{1}{8}\omega^4\theta(s) f(Re_n, \beta) + \omega^2(8\gamma_0 + \theta(s) f(Re_n, \beta) - 2) - 4\omega - 2\theta(s) f(Re_n, \beta) = 0. \tag{B17}$$

If the length L (or the width D) of the rectangular screen is infinitely long then we can show that

$$\lim_{L\to\infty} \gamma_0 = \frac{1}{12}, \tag{B18}$$

and we tend to the 2-D case studied by Steiros & Hultmark (2018).

Appendix C

This appendix contains the details of the experimental data and their processing.

C.1. *Screen samples*

The characteristics of the different porous screens used for the measurement are presented in table 4. They are mainly square wire mesh screens, as represented in figure 22. In addition, five other types of screen were used to test the robustness of the model.

Screen no.	Fibre diameter d (mm)	Reynolds number Re_d	Solidity s	Note
P1	0.29 ± 0.01	186	0.58 ± 0.01	Square woven mesh, nylon fibres
P2	1.1 ± 0.5	705	0.41 ± 0.05	Regular net
P3	1.9 ± 1.0	1218	0.87 ± 0.05	Regular net
P4	0.26 ± 0.01	167	0.61 ± 0.01	Square woven mesh, nylon fibres
P5	0.10 ± 0.01	64	0.56 ± 0.02	Square woven mesh, nylon fibres
P6	0.18 ± 0.02	115	0.61 ± 0.02	Square woven mesh, metal fibres
P7	0.27 ± 0.01	173	0.45 ± 0.01	Square woven mesh, nylon fibres
P8	0.13 ± 0.01	83	0.70 ± 0.01	Square woven mesh, nylon fibres
P9	0.0009–0.019	0.6–12	0.26 ± 0.03	Surgical face mask, physical characteristics
	mean 0.006 ± 0.003	4		according to Monjezi & Jamaati (2021) and Du *et al.* (2021)
P10	0.27 ± 0.01	173	0.11 ± 0.01	Square woven mesh, nylon fibres
P11	0.27 ± 0.01	173	0.37 ± 0.01	Square woven mesh, nylon fibres
P12	0.27 ± 0.01	173	0.31 ± 0.01	Square woven mesh, nylon fibres
P13	0.27 ± 0.01	173	0.17 ± 0.01	Square woven mesh, nylon fibres
P14	0.27 ± 0.01	173	0.24 ± 0.01	Square woven mesh, nylon fibres
P15	0.27 ± 0.01	173	0.24 ± 0.01	Square woven mesh, nylon fibres
P16	0.27 ± 0.01	173	0.24 ± 0.01	Square woven mesh, nylon fibres
P17	0.27 ± 0.01	173	0.15 ± 0.01	Square woven mesh, nylon fibres
P18	0.27 ± 0.01	173	0.28 ± 0.01	Square woven mesh, nylon fibres
P19	0.26 ± 0.01	167	0.52 ± 0.01	Square woven mesh, nylon fibres
P20	0.26 ± 0.01	167	0.42 ± 0.01	Square woven mesh, nylon fibres
P21	0.26 ± 0.01	167	0.32 ± 0.01	Square woven mesh, nylon fibres
P22	0.050 ± 0.002	32	0.65	Square woven mesh, homogeneous, polyamide fibres
P23	0.025 ± 0.002	16	0.82	Square woven mesh, homogeneous, polyamide fibres
P24	0.030 ± 0.002	19	0.75	Square woven mesh, homogeneous, polyamide fibres
P25	0.037 ± 0.002	24	0.70	Square woven mesh, homogeneous, polyamide fibres
P26	0.44 ± 0.01	282	0.405 ± 0.002	Parallel nylon fibres
P27	0.12 ± 0.01	38	0.115 ± 0.002	Parallel nylon fibres
P28	0.44 ± 0.01	141	0.114 ± 0.002	Parallel nylon fibres
P29	0.02 ± 0.002	6	0.080 ± 0.002	Parallel copper fibres
P30	0.44 ± 0.01	282	0.080 ± 0.001	Parallel nylon fibres
P31	—	—	1.00	Flat plate, thickness 0.1 mm

Table 4. Porous screen characteristics. The Reynolds number Re_d is calculated with a velocity $v_0 = 10\,\mathrm{m\,s^{-1}}$ and a kinematic viscosity $\nu = 15.6 \times 10^{-6}\,\mathrm{m^2\,s^{-1}}$, except for the screens P27, P28 and P29 where the velocity is $v_0 = 5\,\mathrm{m\,s^{-1}}$.

C.2. *Correction of the coupling drag*

Due to the mast and frame supporting the porous structure, to obtain the drag coefficient of the porous structure from the raw data composed of the measured forces denoted F_{t+m}, the contributions of each part must be decoupled.

In our analysis of the data, we consider the most simple assumption that the coupling is negligible. Therefore, the drag force of the porous screen is the drag force of the total system (mast, frame and porous screen) minus the drag force of the mast and the frame (without the porous screen, measured before the series of measurements). In order to justify this assumption, we estimated the coupling drag force (the additional term due to the interference between the frame and the screen) for what we assumed to be the worst case, that is, for the solidity equal to 1.

As far as we know, this coupling is nonlinear and there is no general method. We adopt the approach we detail here, based on different measurements with and without the frame illustrated in figure 23. Due to the elongated shape of the mast and the way it is connected to the screen, it is reasonable to assume that the drag force of the mast F_m and the rest of the system F_t add up (giving what we denote F_{t+m}). For the frame, the coupling with

Experience	v_0 (m s^{-1})	F_p (N)	F_c (N)	F_t (N)	F_r (N)	Estimation of ΔF (N)	$F_t - F_c$ (N)
Screen at 90°	0.51	0.002	0.002	0.004	0.003	0.000	0.002
	1.02	0.008	0.003	0.011	0.010	0.000	0.008
	4.00	0.101	0.022	0.118	0.122	−0.005	0.096
	5.03	0.159	0.036	0.185	0.191	−0.010	0.149
	5.98	0.221	0.052	0.260	0.272	−0.013	0.208
	7.00	0.301	0.072	0.350	0.370	−0.023	0.278
	8.02	0.398	0.095	0.467	0.490	−0.026	0.372
	8.97	0.495	0.118	0.588	0.606	−0.025	0.470
	9.99	0.620	0.144	0.710	0.750	−0.054	0.566
	11.01	0.753	0.173	0.862	0.919	−0.064	0.689
	12.03	0.897	0.208	1.024	1.092	−0.081	0.816
	12.98	1.042	0.240	1.178	1.262	−0.104	0.938
Drag coefficient C_D	—	0.993	—	0.973	0.986	—	0.939

Table 5. Summary of the values of the coupling drag force for a flat plate (solidity $s = 1$) for different velocities. All the values have an uncertainty of approximately 0.020 N. For the measurement of F_p and F_r, a solid flat plate with 4.0 mm thickness has been used, corresponding to the thickness of the frame used for measuring F_c and F_t. The drag coefficients are obtained using the dimensions shown in figure 23 with fluid density estimated from the measurement of temperature, pressure and humidity during the different experiments.

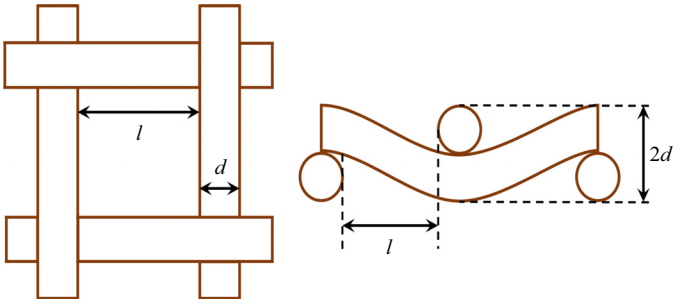

Figure 22. Diagram of the fibre mesh.

the porous structure is expected to be more important. We measured the drag force of the mast alone F_m and subtracted the value of F_{t+m}. We measured the drag force of the mast alone F_m and substracted it from the total force F_{m+t}. The drag force of the porous screen is denoted F_p and the coupling term is denoted ΔF. The total force measured of the frame and the porous screen F_t can be written as

$$F_t = F_c + F_p + \Delta F. \tag{C1}$$

To determine the coupling (or interference) term ΔF, we know exactly the value of the drag force of the porous structure for two points: the first at solidity $s = 0$ where $F_p = 0$, and the second at solidity $s = 1$ for which we can determine easily the drag force without a frame since we can use a solid plate with the same surface area and thickness.

Note that the value of the coupling is not independent of the solidity: indeed, if we assume a monotone dependency, then the lower the solidity, the lower the coupling will be, until it reaches a zero value at zero solidity. These two points allow us to estimate the coupling.

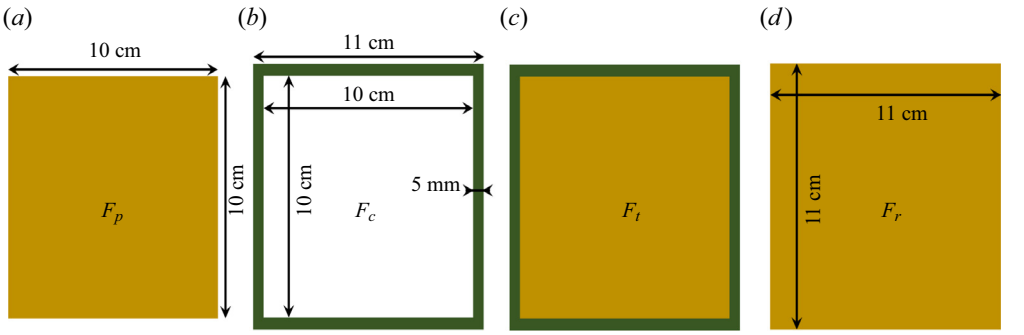

Figure 23. Diagram of the screens (in dark gold) and the frame support (in green).

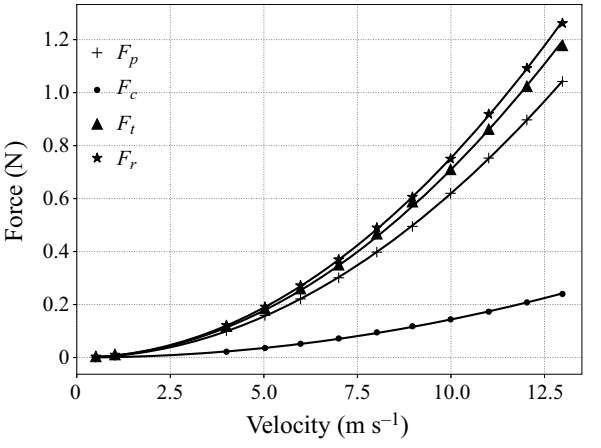

Figure 24. Drag force for the plates and the frame represented in figure 23. Values and drag coefficients are in table 5. Data are fitted using a quadratic law with respect to the velocity v_0. The surface is orthogonal to the mean far-field flow direction $\boldsymbol{v}_0$.

The frame has a thickness of 0.2 mm each side of the system. Therefore, to quantify the influence of this extrusion on the drag force, we measured for the solidity $s = 1$, the drag force F_r of a plate in figure 23(d) and the drag force F_t of the system composed of the frame and the porous screen in figure 23(c), with the same width at the border. The drag forces are shown in table 5 and in figure 24.

We notice that correcting our data with a constant coupling (interference) drag term would not change the curve shape. Doing so with a linear coupling would have a minor effect. Indeed, if the use of a frame to stretch the textiles seems to underestimate the drag coefficient, the difference for the worst case in the drag coefficient between the screen measured directly (0.993) and the screen measured with the frame after subtraction of its drag force (0.939) is closed to the order of the uncertainty calculated in the next section. Even if we added the coupling drag force estimated for solidity 1 in all our data, this would not change our conclusions. Therefore, it is reasonable to neglect the interference drag, and simply proceed with the subtraction of the frame drag force from the total drag force.

C.3. *Determination of the drag coefficient*

To determine the drag coefficient, we calculate a nonlinear regression of the corrected data with the method of the least squares. The model function is

$$F_{p_i} = f(v_i, C_D) = \tfrac{1}{2}\rho S_p C_D v_i^2, \tag{C2}$$

where C_D is the adjustable parameter. We minimize the sum of the square residuals S,

$$S = \sum_{i=1}^{n} (y_i - f(v_i, C_D))^2. \tag{C3}$$

This leads to

$$C_D = \frac{2}{\rho S} \frac{\sum_{i=1}^{n} F_{p_i} v_i^2}{\sum_{i=1}^{n} v_i^4}. \tag{C4}$$

C.4. *Measurement uncertainty*

In what follows, we estimate the measurement uncertainty u of the physical quantities. We assume, for simplicity, that the parameters ρ, F_{p_i}, v_i and S, for $i \in [\![1, n]\!]$ are mutually independent, and that their respective uncertainty is small compared with their value. We neglect the uncertainty on the velocity, then the uncertainty can be calculated with

$$u^2(C_D) = \frac{4}{\rho^2 S^2 \left(\sum_{i=1}^{n} v_i^4\right)^2} \left(\left(\sum_{i=1}^{n} F_{p_i} v_i^2\right)^2 \left(\frac{u^2(\rho)}{\rho^2} + \frac{u^2(S)}{S^2} \right) + \sum_{i=1}^{n} v_i^4 u^2(F_{p_i}) \right). \tag{C5}$$

We assume that the force uncertainty is the same for all the data, this assumption is supported by the different repeated measurements we performed for several porous screens, we take the mean value of the deviation we obtained for the force uncertainty.

C.4.1. *Solidity uncertainty*

The solidity of the porous screens with a regular nylon woven mesh are determined using an image of the screen at the scale of a hundred meshes, taken with a microscope. Several image analyses are used to estimate the solidity and the associated uncertainty. The uncertainty is estimated to ± 0.02.

C.4.2. *Parameter and drag force uncertainties*

The uncertainty of the drag force arises from the error of the force balance. By repeating the measurement several times, for different porous screens, we estimated the drag force uncertainty to approximately ± 0.02 N. The uncertainty of the air density is $\pm 0.005\,\mathrm{kg\,m^{-3}}$. Finally, the uncertainty on the surface of the screen is estimated to $\pm 4 \times 10^{-6}\,\mathrm{m^2}$.

References

Ando, S., Nishikawa, M., Kaneda, M. & Suga, K. 2022 Numerical simulation of filtration processes in the flow-induced deformation of fibrous porous media by a three-dimensional two-way fluid–structure interaction scheme. *Chem. Engng Sci.* **252**, 117500.

Apelt, C.J. & West, G.S. 1974 The effects of wake splitter plates on bluff-body flow in the range $10^4 < Re < 5 \times 10^4$. Part 2. *J. Fluid Mech.* **71**, 145–160.

Ayati, A.A., Steiros, K., Miller, M.A., Duvvuri, S. & Hultmark, M. 2019 A double-multiple streamtube model for vertical axis wind turbines of arbitrary rotor loading. *Wind Energy Sci.* **4** (4), 653–662.

Bailey, B.J., Montero, J.I., Parra, J.P., Robertson, A.P., Baeza, E. & Kamaruddin, R. 2003 Airflow resistance of greenhouse ventilators with and without insect screens. *Biosyst. Engng* **86** (2), 217–229.

Blevins, R.D. 1992 *Applied Fluid Dynamics Handbook*. Krieger Publishing.

Bourrianne, P., Xue, N., Nunes, J., Abkarian, M. & Stone, H.A. 2021 Quantifying the effect of a mask on expiratory flows. *Phys. Rev. Fluids* **6** (11), 110511.

de Bray, B.G. 1957 Low speed wind tunnel tests on perforated square flat plates normal to the airstream: drag and velocity fluctuation measurements. *Current Paper* 323. Ministry of Supply, Aeronautical Research Council.

Brundrett, E. 1993 Prediction of pressure drop for incompressible flow through screens. *J. Fluids Engng* **115** (2), 239–242.

Carvajal, D., Silva-Llanca, L., Larraguibel, D. & González, B. 2020 On the aerodynamic fog collection efficiency of fog water collectors via three-dimensional numerical simulations. *Atmos. Res.* **245**, 105–123.

Cheer, A.Y.L. & Koehl, M.A.R. 1987 Paddles and rakes: fluid flow through bristled appendages of small organisms. *J. Theor. Biol.* **129**, 17–39.

Crompton, M.J. & Barrett, R.V. 2000 Investigation of the separation bubble formed behind the sharp leading edge of a flat plate at incidence. *Proc. Inst. Mech. Engrs* G **214** (3), 157–176.

de Dios Rivera, J. 2011 Aerodynamic collection efficiency of flog collectors. *Atmos. Res.* **102**, 335–342.

Du, W., Iacoviello, F., Fernandez, T., Loureiro, R., Brett, D.J.L. & Shearing, P.R. 2021 Microstructure analysis and image-based modelling of face masks for Covid-19 virus protection. *Commun. Mater.* **2** (69), 217–229.

Eckert, B. & Pflüger, F. 1942 The resistance coefficient of commercial round wire grids. *Technical Memorandum* 1003. National Advisory Committee for Aeronautics.

Fail, R., Lawford, J.A. & Eyre, R.C.W. 1957 Low-speed-experiments on the wake characteristics of flat plates normal to an air stream. *Rep. and Memoranda* 3120. Aeronautical Research Council.

Giannoulis, A., Stathopoulos, T., Briassoulis, D. & Mistriotis, A. 2012 Wind loading on vertical panels with different permeabilities. *J. Wind Engng Ind. Aerodyn.* **107–108**, 1–16.

Gunter, N.M. 1967 *Potential Theory and its Application to Basic Problems of Mathematical Physics*. Frederick Ungar.

Hoerner, S.F. 1952 Aerodynamic properties of screens and fabrics. *Textile Res. J.* **22** (4), 274–280.

Hoerner, S.F. 1965 *Fluid Dynamic Drag*. Published by the Author.

Hood, K., Jammalamadaka, M.S.S. & Hosoi, A.E. 2019 Marine crustaceans with hairy appendages: role of hydrodynamic boundary layers in sensing and feeding. *Phys. Rev. Fluids* **4**, 114102.

Ito, A. & Garry, K.P. 1998 Pressure measurements around a two-dimensional gauze at incidence. *J. Fluids Struct.* **12**, 171–181.

Johari, H. & Desabrais, K.J. 2005 Vortex shedding in the near wake of a parachute canopy. *J. Fluid Mech.* **536**, 185–207.

Kalugin, V.T., Epikhin, A.S., Chernukha, P.A. & Kalugina, M.D. 2021 The effect of perforation on aerodynamic characteristics and the vortex flow field around a flat plate. *IOP Conf. Ser.* **1191**, 1–7.

Koo, J.-K. & James, D.F. 1973 Fluid flow around and through a screen. *J. Fluid Mech.* **60**, 513–538.

Kress, R. 1999 *Linear Integral Equations*, Applied Mathematical Sciences, vol. 82. Springer.

Laws, E.M. & Livesey, J.L. 1978 Flow through screens. *Ann. Rev. Fluid Mech.* **10**, 247–266.

Ledda, P.G., Boujo, E., Camarri, S., Gallaire, F. & Zampogna, G.A. 2021 Homogenization-based design of microstructured membranes: wake flow past permeable shells. *J. Fluid Mech.* **927**, A31.

Ledda, P.G., Siconolfi, L., Viola, F., Gallaire, F. & Camarri, S. 2018 Suppression of von Kármán vortex streets past porous rectangular cylinders. *Phys. Rev. Fluids* **3**, 103901.

Letchford, C.W. 2001 Wind loads on rectangular signboards and hoardings. *J. Wind Engng Ind. Aerodyn.* **89**, 135–151.

Mittal, R., Ni, R. & Seo, J.-H. 2020 The flow physics of Covid-19. *J. Fluid Mech.* **894**, F2.

MONCUQUET, A., MITRANESCU, A., MARCHAND, O.C., RAMANANARIVO, S. & DUPRAT, C. 2022 Collecting fog with vertical fibres: combined laboratory and in-situ study. *Atmos. Res.* **277**, 106312.

MONJEZI, M. & JAMAATI, H. 2021 The effects of face mask specifications on work of breathing and particle filtration efficiency. *Med. Engng Phys.* **98**, 36–43.

OKAMOTO, M. & AZUMA, A. 2011 Aerodynamic characteristics at low Reynolds numbers for wings of various planforms. *AIAA J.* **49** (6), 1135–1150.

O'NEILL, F.G. 2006 Source models of flow through and around screens and gauzes. *Ocean Engng* **33**, 1884–1895.

PARKINSON, G.V. & JANDALI, T. 1970 A wake source model for bluff body potential flow. *J. Fluid Mech.* **40**, 577–594.

PEZZULLA, M., STRONG, E.F., GALLAIRE, F. & REIS, P.M. 2020 Deformation of porous flexible strip in low and moderate Reynolds number flows. *Phys. Rev. Fluids* **5**, 084103.

PINKER, R.A. & HERBERT, M.V. 1967 Pressure loss associated with compressible flow through square-mesh wire gauzes. *J. Mech. Engng Sci.* **9** (1), 11–23.

POMARANZI, G., DANIOTTI, N., SCHITO, P., ROSA, L. & ZASSO, A. 2020 Experimental assessment of the effects of a porous double skin façade system on cladding loads. *J. Wind Engng Ind. Aerodyn.* **196**, 104019.

PONTAVICE, E.D. 2016 Propulsion par cerf-volant: envol et pérégrinations. PhD thesis, Université Paris-Saclay.

PRANDTL, L. & FLACHSBART, O. 1932 Widerstand von seidengazefiltern, runddraht- und bledistreifensieben mit quadratischen maschen. Ergebnisse der Aerodynamischen Versuchsanstalt zu Göttingen.

PRESSLEY, A. 2010 *Elementary Differential Geometry*. Springer.

REGALADO, C.M. & RITTER, A. 2016 The design of an optimal fog water collector: a theoretical analysis. *Atmos. Res.* **178–179**, 45–54.

REYNOLDS, A.J. 1969 Flow deflection by gauze screen. *J. Mech. Engng Sci.* **11** (65), 290–294.

ROSHKO, A. 1954 A new hodograph for free-streamline theory. *Tech. Note* 3168. National Advisory Committee for Aeronautics.

SARPKAYA, T. & LINDSEY, P.J. 1990 Unsteady flow about porous cambered shells. *J. Aircraft* **28** (8), 502–508.

SCHUBAUER, G.B., SPANGENBERG, W.G. & KLEBANOFF, P.S. 1950 Aerodynamic characteristics of damping screens. *National Advisory Committee for Aeronautics Collection* 2001.

SHKLYAR, A. & ARBEL, A. 2008 Numerical simulations of turbulent flow through screen mesh by transient SST and $k-\epsilon$ turbulent models. *Acta Hortic.* **802**, 61–66.

SIMMONS, M.A. & COWDREY, C.F. 1945 Measurement of the aerodynamic forces acting on pours screens. *Rep. and Memoranda* 2276. National Advisory Committee for Aeronautics.

STEIROS, K., BEMPEDELIS, N. & CICOLIN, M.M. 2022 An analytical blockage correction model for high-solidity turbines. *J. Fluid Mech.* **948**, A57.

STEIROS, K. & HULTMARK, M. 2018 Drag on flat plates of arbitrary porosity. *J. Fluid Mech.* **853**, 1–11.

TAYLOR, G.I. 1944 Air resistance of a flat plate of very porous material. *Rep. and Memoranda* 2236. Aeronautical Research Council.

TAYLOR, G.I. & DAVIES, R.M. 1944 The aerodynamics of porous sheets. *Rep. and Memoranda* 2237. Aeronautical Research Council.

TEITEL, M. 2010 Using computational fluid dynamics simulations to determine pressure drops on woven screens. *Biosyst. Engng* **105**, 172–179.

TORRES, G.E. & MUELLER, T.J. 2004 Low-aspect-ratio wing aerodynamics at low Reynolds numbers. *AIAA J.* **42** (5), 865–873.

WANG, Y., YANG, G., HUANG, Y., HUANG, Y., ZHUAN, R. & WU, J. 2021 Analytical model of flow-through-screen pressure drop for metal wire screens considering the effects of pore structures. *Chem. Engng Sci.* **229**, 116037.

WIEGHARDT, K.E.G. 1953 On the resistance of screens. *Aeronaut. Q.* **4**, 186–192.

WU, T.Y.-T. 1962 A wake model for free-streamline flow theory. Part 1. Fully and partially developed wake flows and cavity flows past an oblique flat plate. *J. Fluid Mech.* **13**, 161–192.

XU, M., PATRUNO, L., LO, Y.-L. & DE MIRANDA, S. 2020 On the use of the pressure jump approach for the simulation of separated external flows around porous structures:a forward facing step. *J. Wind Engng Ind. Aerodyn.* **207**, 104377.

YIH, C.-S. 1957 Stream functions in three-dimensional flows. *La Houille Blanche* **43**, 439–450.

ZAMPOGNA, G.A. & GALLAIRE, F. 2020 Effective stress jump across membranes. *J. Fluid Mech.* **892**, A9.